coatings

MDPI

Article

Low-Temperature Synthesized Mixed-Phase Copper Oxides Deposited for Photocatalytic Antibiotic Degradation

Maria-Anthoniette Oghenetejiro Onoriode-Afunezie [1,*], Arminas Gloveckas [1], Brigita Abakevičienė [2,*] and Agnė Šulčiūtė [1]

[1] Faculty of Chemical Technology, Kaunas University of Technology, Radvilenu Pl. 19, LT-50254 Kaunas, Lithuania
[2] Institute of Materials Sciences, Kaunas University of Technology, K. Barsausko Str. 59, LT-51423 Kaunas, Lithuania
* Correspondence: maria.onoriode@ktu.edu (M.-A.O.O.-A.); brigita.abakeviciene@ktu.lt (B.A.)

Abstract

The persistence of antibiotics like ciprofloxacin (CIP) in aquatic environments necessitates the development of efficient, low-cost wastewater treatment technologies. This study investigates a low-temperature fabrication strategy for mixed-phase copper oxide (CuO/Cu_2O) coatings synthesized via co-precipitation and immobilized using electrophoretic deposition (EPD). A critical finding was that a 25 min precursor aging time (T25) preserved a metastable mixture of CuO and Cu_2O phases, which is highly advantageous for creating heterojunction interfaces that enhance charge separation. In contrast, extended aging (T35) promoted phase consolidation toward bulk CuO, reducing catalytic surface area. During the EPD process, applied voltage acted as an influence to the relative phase composition and deposition behavior of the deposited coatings; 1.0 V was identified as the optimal condition, balancing high phase fidelity with enhanced crystallinity (average crystallite size of 30.6 nm) and mechanical stability. Photocatalytic experiments demonstrated significant CIP degradation, with the 0.9 V and 1.0 V films outperforming the 1.2 V film, possibly due to more favorable surface chemistry and phase diversity. While the 0.9 V film achieved the highest mineralization efficiency (18% TOC removal), the 1.0 V film offered the best balance between photocatalytic activity, structural stability, and phase selectivity for practical applications. High-Performance Liquid Chromatography-Mass Spectrometry HPLC-MS analysis suggested that degradation proceeds through oxidative pathways involving piperazine ring cleavage and defluorination.

Keywords: mixed-phase oxides; electrophoretic deposition; antibiotics; wastewater remediation; photocatalytic degradation

Academic Editors: Feng Wang, Zuoli He and Maria Vittoria Diamanti

Received: 17 June 2026
Revised: 19 July 2026
Accepted: 14 August 2026
Published: 17 August 2026

1. Introduction

Antibiotics such as ciprofloxacin, amoxicillin, and norfloxacin are frequently utilized in clinical, agricultural, and veterinary settings; however, a significant portion of these chemicals are not fully metabolized and are discharged into wastewater systems. Their persistence causes prolonged environmental exposure, the spread of antimicrobial resistance, and ecological damage, making them the main emerging pollutants in aquatic settings. Antibiotic pollution studies highlight the need for new treatment systems that can successfully degrade these chemicals under environmental circumstances [1]. Among these compounds, Ciprofloxacin is frequently detected in wastewater effluents and natural water

bodies because of its chemical stability and resistance to biodegradation. Studies have demonstrated that photocatalytic systems can effectively degrade ciprofloxacin through oxidative pathways involving reactive oxygen species [2].

Advanced Oxidation Processes (AOPs) have emerged as highly efficient methods for the removal of recalcitrant organic pollutants through the generation of non-selective and highly reactive oxygen species (ROS). These processes rely on the in situ production of hydroxyl radicals (·OH) and superoxide anions ($O_2 \cdot^-$), which possess the high oxidation potential necessary to break down complex antibiotic structures like ciprofloxacin into smaller, less toxic fragments. Visible-light photocatalysis using semiconductor heterojunctions is a particularly promising AOP, as it leverages renewable energy to drive these redox reactions. Furthermore, the efficiency of these AOPs is intrinsically linked to the adsorption mechanism; the catalyst surface must exhibit high chemical affinity for the target pharmaceutical to facilitate the subsequent radical-driven mineralization. Recent studies have reported efficient photocatalytic degradation of ciprofloxacin using semiconductor catalysts capable of producing multiple reactive species during illumination, demonstrating the potential of photocatalytic technologies for wastewater remediation [3,4].

Copper-based oxides (mainly cupric oxide, CuO, and cuprous oxide, Cu_2O) are promising for environmental remediation because they exhibit both photocatalytic activity under visible light and broad-spectrum antimicrobial action [5]. Upon light excitation, copper oxides can generate electron–hole pairs that lead to reactive oxygen species (including ·OH and $O_2 \cdot^-$), which are effective in mineralizing organic pollutants, including dyes and antibiotics [6]. The coexistence of CuO and Cu_2O phases is especially advantageous because the formation of heterojunction interfaces between the two semiconductors can enhance charge separation and reduce electron–hole recombination. Such interfacial charge transfer processes, particularly in systems where Cu_2O is deposited on or coexists with CuO, have been shown to significantly improve the efficiency of photocatalytic degradation for organic pollutants and antibiotics [5,7]. Recent work has demonstrated that integrating CuO and Cu_2O thin films forms a visible-light-active heterojunction that increases charge collection, reduces recombination, and outperforms single-phase CuO or Cu_2O for organic pollutant degradation [8].

Conventional synthesis of copper oxides for catalytic or antimicrobial applications often involves high-temperature calcination (300–500 °C) to improve crystallinity. Although calcination increases phase purity, it may simultaneously reduce surface defect density, lower ion-release capacity, and typically result in larger crystallite sizes, all of which can diminish both photocatalytic and antimicrobial performance. Low-temperature synthesis routes, such as co-precipitation, offer an alternative approach that preserves high surface area, abundant defect sites, and metastable mixed-phase compositions [9]. This effect has been observed in studies where non-calcined metal oxide nanostructures show higher surface reactivity compared to extensively heat-treated analogs [9,10].

A critical yet under-explored parameter in co-precipitation synthesis is precursor aging time, which governs crystal nucleation, growth pathways, and defect formation in copper oxide phases. Controlled aging can produce mixed CuO/Cu_2O compositions with enhanced defect densities, potentially leading to improved light absorption, charge separation, and reactive species generation. Moreover, low-temperature synthesis preserves surface functionalities and metastable species that contribute to catalytic activity; in contrast, high-temperature calcination has been shown to eliminate these active states through phase consolidation and loss of surface-adsorbed groups [9]. Once synthesized, the scalable immobilization of these copper oxide nanoparticles onto substrates requires deposition techniques compatible with low-temperature processing.

Electrophoretic deposition (EPD) is a versatile technique for immobilizing nanoparticles onto conductive substrates under the influence of an electric field. EPD offers several advantages over traditional coating methods, including rapid deposition, uniform film formation, and the ability to control film thickness and morphology by adjusting process parameters such as voltage, deposition time, and suspension composition [11,12]. Cathodic EPD of CuO nanoparticle suspensions has been shown to produce controllable coating thickness and morphology, with applied electric fields yielding optimal coatings and linear thickness growth with deposition time [13]. Furthermore, EPD can be performed at room temperature, making it compatible with low-temperature synthesis strategies and enabling the preservation of metastable phases that might otherwise be lost during high-temperature processing [14,15].

The applied voltage during EPD not only influences deposition kinetics but can also influence the relative phase composition and deposition behavior of the deposited coatings, affecting the relative proportions of CuO and Cu_2O in the deposited film. This voltage-dependent phase transfer phenomenon is critical for optimizing the photocatalytic performance of mixed-phase copper oxide coatings. Understanding the relationship between EPD parameters and the resulting phase composition is essential for designing efficient photocatalytic systems [16].

Despite these advances, there is a notable gap in the literature: few studies combine non-calcined copper oxide films deposited by EPD at low voltages ($\leq$1.2 V) onto relevant substrates like glass (FTO) for photocatalytic antibiotic degradation. Most reported systems focus on powders [17] or require high-temperature annealing [17,18], leaving a need for integrated low-temperature fabrication strategies that preserve active surface states.

This study investigates a low-temperature co-precipitation and electrophoretic deposition (EPD) strategy for fabricating high-performance, mixed-phase copper oxide coatings. We hypothesize that a precisely controlled precursor aging window (T25) can produce metastable mixed CuO/Cu_2O compositions that, by preserving diverse defect densities and heterojunction interfaces, facilitate charge separation and reactive species generation compared to over-aged, consolidated CuO phases. Specifically, we examine how precursor chemistry and aging time govern the initial phase composition and how subsequent low-voltage EPD acts as a selective phase-selective mechanism. By establishing this direct link from synthesis kinetics to photocatalytic mineralization pathways, this work offers a scalable, energy-efficient approach for sustainable antibiotic remediation in wastewater treatment applications.

2. Materials and Methods

2.1. Materials

Copper(II) nitrate trihydrate ($Cu(NO_3)_2 \cdot 3H_2O$) (EUROCHEM BGD Sp. z o. o., Tarnów, Poland) and sodium hydroxide (NaOH) (UAB Eurochemicals, Vilnius, Lithuania) were used as the copper precursor and precipitating agent, respectively. Citric acid (UAB Eurochemicals, Vilnius, Lithuania), methanol (EUROCHEM BGD Sp. z o. o., Tarnów, Poland), hydrogen peroxide (UAB Eurochemicals, Vilnius, Lithuania), and deionized water were employed for suspension preparation during electrophoretic deposition. Glass substrates (TEC-15) with a length of 3 cm, width of 1 cm and thickness of 2.2 mm were used as deposition support. All chemicals were of analytical grade and used as received without further purification. Deionized water (resistivity $\geq$ 18.2 MΩ·cm) was used throughout all experiments.

2.2. Synthesis of Copper Oxides via Aging-Controlled Co-Precipitation

The materials used in this study included copper (II) nitrate trihydrate (Cu $(NO_3)_2 \cdot 3H_2O$) as the copper precursor and sodium hydroxide (NaOH) as the precipitating agent, both of analytical grade. A 0.2 M copper nitrate solution was prepared and stirred at room temperature, after which 1.0 M NaOH was also prepared. The synthesis of the mixed-phase copper oxides proceeded by introducing the sodium hydroxide solution dropwise into the stirred copper nitrate precursor to ensure controlled crystal nucleation [19] until complete precipitation was achieved. Once the precipitation was complete, the resulting suspension was immediately transferred to a dark environment to prevent premature photo-reduction and allowed to age for predetermined intervals of 0 min to 60 min. Aging time was defined as the period between completion of precipitation and solid–liquid separation.

Following the aging process, the solid precipitates were recovered via vacuum filtration and subjected to multiple washing cycles with deionized water to eliminate residual nitrate and sodium ions. The obtained solids were dried at 80 °C in a convective oven. No high-temperature calcination was applied to preserve surface defects and mixed copper oxidation states [9]. The dried powder was ground gently using a mortar and pestle to obtain a fine powder for subsequent characterization and EPD.

2.3. Particle Size, Distribution, and Determination of Specific Surface Area

The copper oxide particle size and granulometry were analyzed at various temperatures using a CILAS 1090 LD laser granulometer (CILAS, Orléans, France). Measurements were conducted within a range of 0.1–500 µm with air dispersion at a pressure of 2500 mbar. Solid particles in the air stream were distributed between 10 and 15% at 15 s intervals. The specific surface area was subsequently determined based on the granulometric composition obtained.

2.4. Preparation of EPD Suspensions

To prepare the suspensions for electrophoretic deposition, the dried mixed-phase copper oxide powders were dispersed in a methanol–water binary solvent system specifically formulated for particle dispersion, surface modification, and long-term stabilization. The EPD suspensions were prepared as stable colloidal dispersions using a precisely staged integration sequence to ensure optimal particle stabilization. Initially, 1.4 g of citric acid was dissolved in 35 mL of deionized water. This step established the necessary chemical environment for surface complexation with the incoming oxide. Subsequently, 2.0 g of the dried T25 copper oxide powder was incorporated into the acidified aqueous phase. Given the high specific surface area of the T25 precursor, the citrate anions immediately began to adsorb onto the sub-micron particles (d_{50} = 0.90 µm), modifying the zeta potential and providing the electrostatic and steric stabilization required to prevent agglomeration.

To assist in surface activation and maintain the oxidative environment necessary to stabilize the metastable Cu^+ states, 5 drops of 35% hydrogen peroxide (H_2O_2) were added to the mixture. Following a controlled heating and stirring phase, the heat was switched off, and 15 mL of methanol was introduced to complete the 70:30 water-to-alcohol binary solvent system. The addition of methanol increased wetting of the oxide particles and lowered surface tension, which promoted uniform particle distribution within the solvent system [20]. Citric acid was introduced as a complexing and dispersing agent to enhance electrostatic stabilization by modifying the surface charge of the copper oxide particles, thereby improving suspension stability during electrophoretic deposition [21]. Hydrogen peroxide was incorporated in small quantities to assist in surface activation and to maintain oxidative conditions that favor stable copper oxide surface states in the suspension.

To break down agglomerates and ensure homogeneous particle distribution, the resultant suspensions were ultrasonically treated for a set amount of time before deposition began. This step was crucial in achieving consistent electrophoretic mobility and film formation across tests. The suspension composition remained unchanged throughout the investigation; all deposition trials used the same solvent ratios, ingredient concentrations, and dispersion protocol. By keeping the suspension chemistry constant, any differences in coating morphology, thickness, or photocatalytic performance could be attributed solely to changes in electrophoretic parameters such as applied voltage and deposition time, allowing for a systematic evaluation of process effects without interference from compositional variability.

2.5. Electrophoretic Deposition

Electrophoretic deposition was performed using a standard two-electrode cathodic arrangement. The working electrode consisted of a TEC-15 glass substrate with physical dimensions of 1.0 cm × 3 cm and a thickness of 2.2 mm. To ensure consistency across trials, a defined effective deposition area of 2.0 cm^2 was utilized for the immobilization of the catalyst, with the substrate placed parallel to a copper counter-electrode at a fixed separation distance of 20 mm. Deposition was conducted at precisely controlled applied potentials of 0.9 V, 1.0 V, and 1.2 V for durations ranging from 5 to 20 min. Following the deposition, the coated substrates were gently rinsed with deionized water to remove weakly attached particles and dried at 80 °C to ensure film adherence without inducing thermal phase transformations. No post-deposition heat treatment was used.

2.6. Characterization Techniques

X-ray diffraction (XRD) was performed on the produced copper oxide powders using a Bruker D8 Advance diffractometer (Bruker AXS GmbH, Karlsruhe, Germany) with Cu Kα radiation (λ = 1.5406 Å) to explore their crystalline phase composition, operating at 40 kV and 40 mA. Scans were performed over a 2θ range of 20–80° with a step size of 0.02° and a scan rate of 2° min^{-1}. Phase identification was performed by comparing the observed diffraction peaks with standard JCPDS cards for CuO (JCPDS 48-1548), (JCPDS 05-0661), Cu_2O (JCPDS 05-0667), $Cu(OH)_2$ (JCPDS 35-0505), and Cu (ICDD 785–1326 and JCPDS 04-0836).

Fourier-transform infrared (FTIR) spectroscopy was performed using a PerkinElmer Spectrum 100 spectrometer (PerkinElmer Ltd., Buckinghamshire, UK) in attenuated total reflectance (ATR) mode. Spectra were recorded over the range of 400–4000 cm^{-1} with a resolution of 4 cm^{-1} and 32 scans per spectrum.

Scanning electron microscopy (SEM) images were obtained using a JEOL JSM-7600F field-emission scanning electron microscope (JEOL Ltd., Tokyo, Japan) operated at 5 kV to examine surface morphology and microstructural features. Energy-dispersive X-ray spectroscopy (EDS) was performed using an Oxford Instruments X-Max detector attached to the SEM to determine elemental composition.

The cross-sectional layer thickness of the electrodeposited films was characterized using a Zeiss Discovery V12 Stereo Microscope equipped with a PlanApo S 1.5× objective lens and PL 10×/23 Br. foc eyepieces. Images were captured within a magnification range of 12× to 150×, utilizing a maximum numerical aperture of 0.144. The system's field of view (19 mm to 1.5 mm) and free working distance (30 mm) allowed for high-resolution imaging of the coating profiles on the glass substrates.

2.7. Adsorption and Photocatalytic Degradation Experiments

The photocatalytic activity was assessed using methylene blue (MB) as a standardized model organic pollutant to establish the intrinsic photocatalytic baseline and optimize

EPD parameters before moving to the more complex ciprofloxacin molecule (CIP) which was a typical antibiotic agent. The initial CIP concentration of 1 mg/L utilized in the adsorption study was chosen to represent the elevated amounts occasionally recorded in hospital and pharmaceutical wastewater, which normally range from nanograms per liter (ng/L) to low milligrams per liter (mg/L). This decision provides observable photocatalytic activity in a controlled laboratory environment using a UV-Vis spectrophotometer while remaining relevant to real-world wastewater treatment conditions [4]. Experiments were carried out in synthetic aqueous solutions (spiked deionized water) and spiked wastewater matrices (biologically treated wastewater) under UV illumination. UV irradiation was selected to provide controlled and reproducible irradiation conditions for comparing the photocatalytic performance of the coatings. Although CuO and Cu_2O exhibit visible-light absorption, standardized UV illumination minimizes variations associated with natural sunlight while allowing a systematic evaluation of catalyst performance.

Prior to illumination, the catalyst-coated substrates were immersed in the pollutant solution and left in the dark to achieve adsorption–desorption equilibrium. Photocatalytic experiments exposed samples to ultraviolet (UV) light using an Aqua Forte 9 W UV-C lamp emitting at a primary wavelength of 254 nm with an irradiation intensity of 3.2 mW/cm^2, a professional water product produced by SIBO Fluidra, Netherlands. The samples were collected at regular intervals and examined using UV-Vis spectroscopy.

The UV–Vis absorption spectra of methylene blue (MB) and ciprofloxacin (CIP) were recorded prior to the photocatalytic experiments to determine their characteristic absorption maxima used for concentration monitoring. As shown in Figure 1, MB exhibits its principal absorption band in the visible region (≈664–666 nm), while CIP displays characteristic absorption bands in the ultraviolet region at approximately 238 and 278 nm.

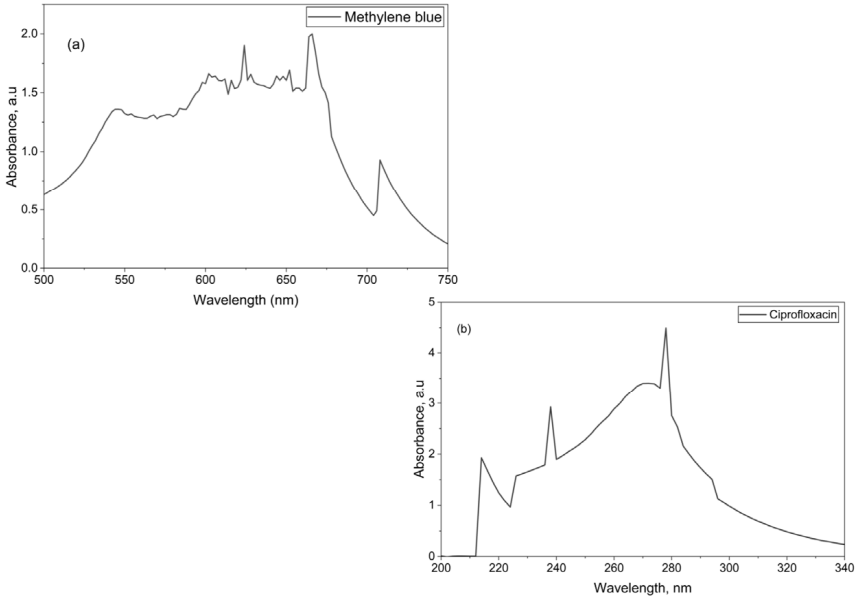

Figure 1. UV–Vis absorption spectra of (**a**) methylene blue and (**b**) ciprofloxacin used to determine the analytical wavelengths employed for photocatalytic degradation measurements.

These wavelengths were subsequently used to monitor concentration changes during the adsorption and photocatalytic degradation experiments. MB degradation was monitored at its typical absorption wavelength (665 nm), whereas ciprofloxacin degradation was recorded by tracking changes in its distinctive UV-Vis absorption bands at 277 nm.

2.8. Reusability and Stability of the Cu Photocatalyst

Cyclic reuse studies were carried out to investigate the reusability and stability of the photocatalysts produced in this study at 0.9 V, 1.0 V, and 1.2 V. Cyclic and reusability experiments in photocatalytic wastewater treatment are critical for determining the long-term effectiveness, stability, and degradation resistance of photocatalysts, ensuring cost-effective and sustainable water treatment. The degradation of CIP was assessed by monitoring the C/C_0 ratios over five consecutive runs within the reactor.

2.9. HPLC-MS Analysis of Degradation Products

We used high-performance liquid chromatography-mass spectrometry (HPLC-MS) to trace the breakdown pathway of ciprofloxacin (CIP) in wastewater. The mass spectra were obtained using an LCMS-2020 (ESI+) (Shimadzu, Kyoto, Japan) instrument outfitted with an ultraviolet detector and a mass spectrometer. The HPLC used a reversed-phase C-Ph column (4.6 mm × 100 mm) to separate polar and nonpolar substances depending on their hydrophobicity.

HPLC separation was achieved using a mobile phase of acetonitrile and water +0.1% formic acid, gradient conditions, and a flow rate of 0.6 mL/min. The mass spectrometer operated in positive and negative ionization modes, allowing for the detection of primary molecular ions and distinctive fragments of ciprofloxacin (CIP) and its derivatives over a wide mass spectrum. This arrangement allowed for detailed monitoring, with CIP being detected at 254 nm for precise quantification. The combination of HPLC and mass spectrometry provides a reliable technology for identifying CIP and its degradation products, offering important insights into the compound's dynamics and transformation during photodegradation.

Samples obtained at regular intervals during photocatalytic degradation trials were examined to determine the absence of CIP. The degradation pathway was reconstructed using the temporal patterns of these intermediates, providing precise information about the mechanisms of CIP breakdown in 0.9 V, 1.0 V, and 1.2 V catalysts.

2.10. Analysis of Total Organic Carbon

A (TOC) analyzer (Shimadzu TOC-L, Shimadzu Ltd., Kyoto, Japan) was used for the quantification of TOC in reactor samples according to the procedure described in the EN1484:2002 standard. TOC removal efficiency was calculated as:

$$\text{TOC removal (\%)} = [(TOC_0 - TOC_t)/TOC_0] \times 100$$

where TOC_0 is the initial TOC and TOC_t is the TOC at time t.

2.11. Quantification of Copper Leaching

The chemical stability and environmental safety of the photocatalytic films were evaluated by monitoring copper ion leaching using an Optical Emission Spectrometer Optima 8000 (PerkinElmer Instruments Co., Waltham, MA, USA). High-purity Argon was utilized as the ICP torch gas at a flow rate of 7.0 L/min and as the purge gas at 1.0 L/min. To ensure measurement precision and system longevity, a recirculating cooling system (chiller) was employed with a cooling capacity of 2850 watts at 20 °C, a temperature stability of ±0.5 °C, and a maximum pump rate of 4 gal/min at 55 psi. Copper concentrations were measured at the characteristic 327.393 nm wavelength to ensure high sensitivity and minimal spectral interference during the 60 min photocatalytic cycles.

3. Results and Discussions

3.1. Morphological and Structural Characterization

3.1.1. XRD Analysis of Precursor Powders

X-ray diffraction analysis was performed to determine the crystalline phases present in the copper oxide precursor powders obtained after aging times of 25 min (T25) and 35 min (T35) prior to isolation and drying. The XRD analysis in Figure 2 reveals that sample T25 exhibits a more complex multi-phase composition compared to T35, with nineteen distinct diffraction peaks indicating the coexistence of multiple copper species. The T25 pattern shows characteristic reflections assignable to tenorite CuO as the dominant phase, with strong peaks at 33.54° ($\bar{1}11$) and 38.85° (111) matching the reported CuO reflections at 35.6° and 38.7° (JCPDS 05-0661) [22,23]. Additional peaks at 29.54°, 42.64°, and the cluster near 40–42° correspond to cuprite Cu_2O (JCPDS 05-0667), while reflections around 48–50° suggest the presence of metallic copper (JCPDS 04-0836) [24–26]. Notably, T25 retains unique fingerprints for metastable $Cu(OH)_2$ at 16.69° (020) and 22.88° (021), alongside a distinct CuO signature at ~48° assigned to CuO (020) (matching JCPDS 05-0661). The extensive peak distribution across 16.69° to 75.17° demonstrates multiple crystallographic planes including contributions from $Cu(OH)_2$, (002), CuO ($\bar{1}11$), (111), (020), (202), ($\bar{1}13$), (220), and (311) planes, Cu_2O (110), (111), (200), and (220) planes, as well as metallic Cu (111) orientations, indicating a heterogeneous film with rich phase diversity [22–25].

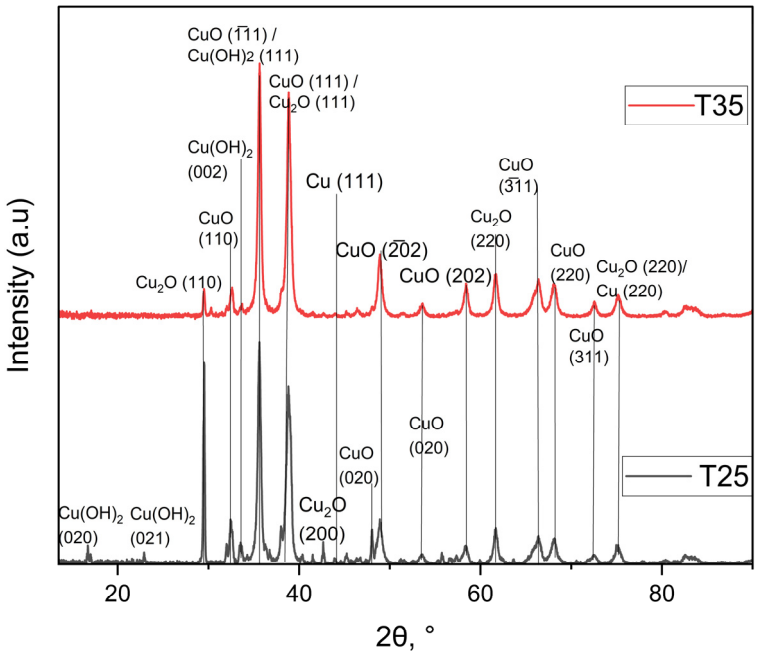

Figure 2. X-ray diffraction (XRD) patterns illustrating the structural evolution of copper oxide precursor powders at different aging intervals. Phase identification is indexed to JCPDS 05-0661 (CuO), JCPDS 05-0667 (Cu_2O), and JCPDS 04-0836 (Cu), showing the transition from a metastable multi-phase composite to a consolidated oxide structure.

While the synthesis utilizes a low-temperature drying step (80 °C), visual observations during the room-temperature dark-aging windows—specifically the blue-to-black color transition—suggest that the thermodynamic driving force for the $Cu(OH)_2 \rightarrow$ CuO dehydration is active before the drying process. In contrast, the T35 analog shows significant phase consolidation toward bulk CuO, evidenced by a reduction to thirteen peaks and the suppression of metastable hydroxide and metallic signals as the material ripens.

In contrast, sample T35 displays thirteen diffraction peaks with a more crystalline and phase-pure character dominated by CuO. The characteristic CuO reflections at 35.64°, 35.77°, and 38.85° are sharper and more intense than in T25, suggesting improved crystallinity and preferential CuO formation [22,23]. While T35 retains some secondary phases evidenced by peaks at 29.52° (Cu_2O), 48.94° (CuO), and higher-angle reflections at 61.5°, 66.46°, 68.29°, and 75.19°, the overall pattern indicates a less heterogeneous composition with fewer overlapping phases compared to T25 [22,23,26]. The reduced number of peaks and enhanced peak intensities in T35 suggest that the extended aging time promotes phase consolidation toward CuO, whereas T25's lower aging conditions preserve a metastable mixture of Cu, Cu_2O, and CuO phases with greater structural complexity and a broader distribution of crystallographic orientations [22–26].

Although both samples exhibit similar phase compositions, significant differences in peak shape and intensity are observed between the two aging conditions. The T35 sample shows noticeably sharper and more intense diffraction peaks, indicating the formation of larger and more highly crystalline particles during the longer aging period [27,28]. In contrast, the T25 sample exhibits broader diffraction peaks with slightly lower intensities, suggesting the presence of smaller crystallites and a higher degree of structural dispersion [27,28].

Peak broadening in the T25 sample is indicative of nanocrystalline domains, which are typically associated with increased surface area and a greater density of active surface sites [27,28]. Such characteristics are beneficial for photocatalytic processes because smaller crystallites can enhance pollutant adsorption and facilitate surface redox reactions [28–30]. In contrast, the increased peak sharpness observed for T35 suggests crystal growth and partial particle aggregation, which may reduce the number of accessible catalytic sites [27,31].

Another important observation is the relative balance between Cu_2O and CuO reflections. The T25 sample shows a more balanced intensity distribution between the two phases, whereas the T35 sample appears to be dominated by a few highly intense reflections, indicating preferential crystal growth of specific orientations [30,32]. A more evenly distributed phase structure is desirable because the coexistence of CuO and Cu_2O can promote interfacial charge transfer between the two semiconductors, improving charge separation and photocatalytic activity [33–36]. Independent synthesis batches prepared using the same procedure exhibited consistent diffraction features, indicating the reproducibility of the precursor synthesis.

The initial precipitation of $Cu(NO_3)_2$ with NaOH is expected to produce $Cu(OH)_2$. However, systematic XRD and FTIR analyses revealed progressive phase evolution during precursor aging and low-temperature drying, resulting in mixed CuO/Cu_2O phases. A detailed discussion of the proposed phase evolution, together with supporting XRD patterns, and literature comparison [37–41], is provided in Supplementary Materials (Figures S1–S4).

The precise mechanism responsible for the formation of the mixed CuO/Cu_2O phases under the present low-temperature processing conditions requires further investigation. In this work, phase identification is based on experimental characterization of the final materials, while the formation pathway is discussed as a plausible interpretation supported by the available literature.

These findings demonstrate that aging time is a critical parameter for controlling phase composition and crystallite size in low-temperature copper oxide synthesis.

3.1.2. FTIR Analysis of Precursor Powders

Fourier transform infrared spectroscopy was utilized to examine the bonding environments and functional groups found in the produced powders. In Figure 3, T25 and T35 samples showed absorption bands between 400 and 600 cm^{-1}, indicating Cu–O lattice

vibrations in copper oxide structures. These bands are generally attributed to stretching modes of Cu–O bonds in CuO and Cu_2O phases, and they support the formation of copper oxide species in the produced materials.

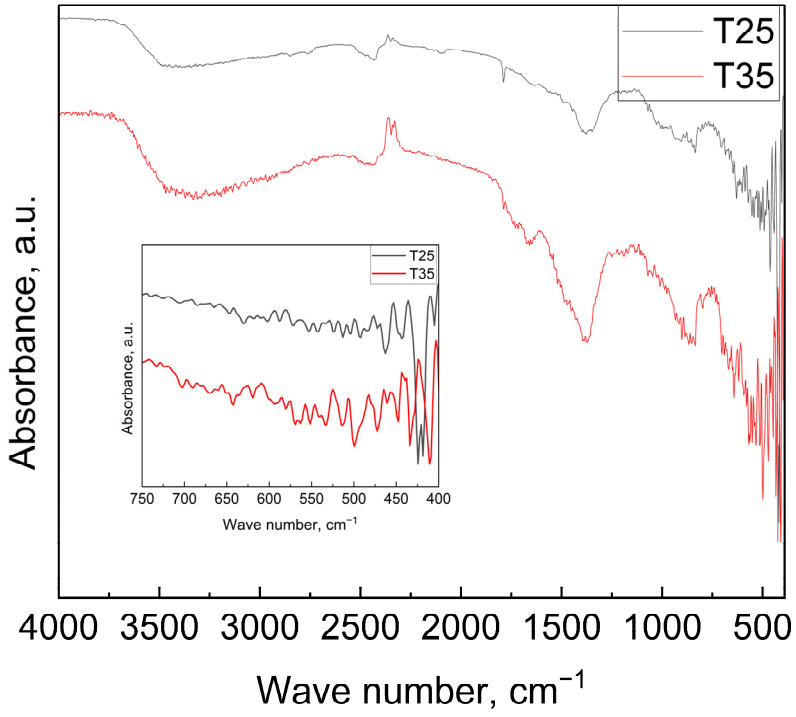

Figure 3. FTIR spectra of T25 and T35 copper oxide precursors.

The FTIR spectrum of the T25 sample reveals a rich distribution of Cu–O vibrational modes across the fingerprint region (400–650 cm^{-1}), indicating a heterogeneous mixed-phase composition favorable for photocatalytic applications. Multiple absorption bands at 424.33, 433.97, 441.79, 493.76, 513.05, 522.69, and 601.77 cm^{-1} correspond to characteristic Cu–O stretching and bending vibrations of tenorite CuO, matching literature-reported modes at 432, 473, 491, 511, 519, and 611 cm^{-1} [42–44]. Critically, the T25 sample exhibits a distinct peak at 628.78 cm^{-1} that aligns precisely with the cuprite Cu_2O vibrational band reported at 624–628 cm^{-1}, supporting the coexistence of both CuO and Cu_2O phases [43]. This mixed-phase structure is highly advantageous for photocatalytic performance because Cu_2O/CuO heterojunctions facilitate interfacial charge transfer, improve electron-hole separation, and enhance visible-light absorption [29,33,34]. The broader distribution of multiple Cu–O vibrational modes in T25 suggests smaller crystallite domains with higher structural disorder, which translates to increased surface area and a greater density of active catalytic sites [27,28]. Additional peaks at 846.73, 1377.14, and 2366.61–2424.47 cm^{-1} indicate the presence of surface-adsorbed species such as carbonates and CO_2, which are indicative of reactive surface sites capable of pollutant adsorption—a critical prerequisite for efficient photocatalytic degradation [35]. The shorter aging time of 25 min preserves these metastable surface states and prevents excessive crystal growth, thereby maintaining the high surface reactivity essential for photocatalytic antibiotic degradation applications.

The FTIR spectrum of the T35 sample displays fewer and more defined absorption bands in the fingerprint region, with prominent peaks at 472.55, 499.55, and 514.98 cm^{-1} corresponding to Cu–O stretching vibrations characteristic of crystalline CuO at 473, 491, and 511 cm^{-1}, respectively [42,43]. However, the T35 spectrum notably lacks a clear Cu_2O signature peak near 624–628 cm^{-1}, with the closest feature appearing at 642.28 cm^{-1}—significantly shifted beyond the reported cuprite range [43]. This absence or

weakening of the Cu_2O phase suggests that the extended 35 min aging period promotes phase transformation toward a more CuO-dominated structure, reducing the beneficial Cu_2O/CuO heterojunction interfaces that are critical for enhanced charge separation and photocatalytic efficiency [29,33,34]. The reduced number of distinct Cu–O vibrational modes compared to T25 indicates a more homogeneous, crystalline CuO phase with larger particle sizes and lower structural diversity, which correlates with decreased surface area and fewer active catalytic sites [27,28]. While T35 exhibits additional bands at 800.44, 837.09, 900, 1049.25, 1377.14, and 1647.17 cm^{-1} that may correspond to carbonate species and adsorbed water, the overall spectral profile suggests a more ordered, less reactive surface compared to T25. The extended aging time allows for crystal ripening and phase consolidation, which diminishes the metastable Cu_2O phase and reduces the interfacial area between CuO and Cu_2O [31,35]. Consequently, T35 exhibits characteristics more aligned with bulk crystalline CuO rather than the nanostructured, mixed-phase composition optimal for photocatalytic applications, making it less suitable for efficient pollutant degradation compared to the T25 sample.

3.1.3. Granulometric Analysis

The granulometric analysis of the synthesized copper oxide precursors, conducted using a CILAS 1090 LD laser granulometer, reveals a well-defined sub-micron particle size distribution. The cumulative volume distribution in Figure 4 indicates a median diameter (d_{50}) of 0.90 µm, with 10% of the particles (d_{10}) measuring below 0.20 µm and 90% (d_{90}) falling below 2.65 µm. The resulting mean diameter of 1.25 µm suggests that the co-precipitation and controlled aging strategy effectively prevents excessive bulk aggregation, maintaining a particle profile that is highly conducive to stable colloidal suspension for the subsequent deposition process.

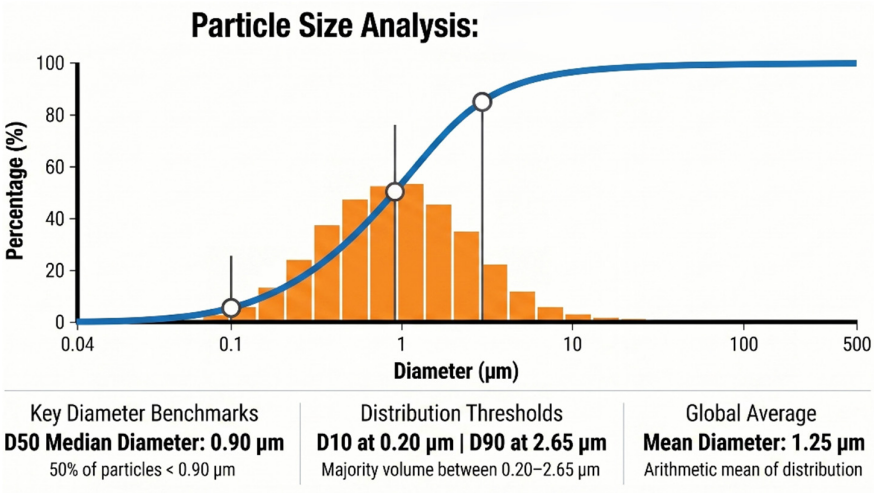

Figure 4. Particle size distribution and granulometric analysis of T25 precursor.

Based on this granulometric composition, the calculated specific surface area is 23,955.20 cm^2/g. This high surface area is consistent with the nanocrystalline domains identified in the XRD analysis of the T25 precursor and is a critical factor for the effective immobilization of particles during electrophoretic deposition. The presence of a significant population of particles in the sub-micron range enhances the electrostatic stabilization provided by citric acid, facilitating the formation of uniform, interconnected particle networks on the glass substrates. Such high surface-to-volume ratios are essential for maximizing the density of active catalytic sites and promoting the efficient adsorption of complex molecules like ciprofloxacin.

3.1.4. SEM Analysis After Electrophoretic Deposition

SEM micrographs in Figure 5 reveal the formation of continuous copper oxide films characterized by a distinctive "mud-crack" morphology. This surface patterning is primarily attributed to the rapid evaporation of the methanol solvent during the low-temperature drying process at 80 °C, which induces capillary stresses that result in micro-cracking across the colloidal particle network [4]. At 0.9 V, the surface exhibits a dense and rough interconnected network composed of bulky clusters, visually corroborating the measured layer thickness of 0.04–0.09 mm. In contrast, the 1.2 V film appears significantly flatter and less consolidated, aligning with its minimal physical thickness of 0.01 mm.

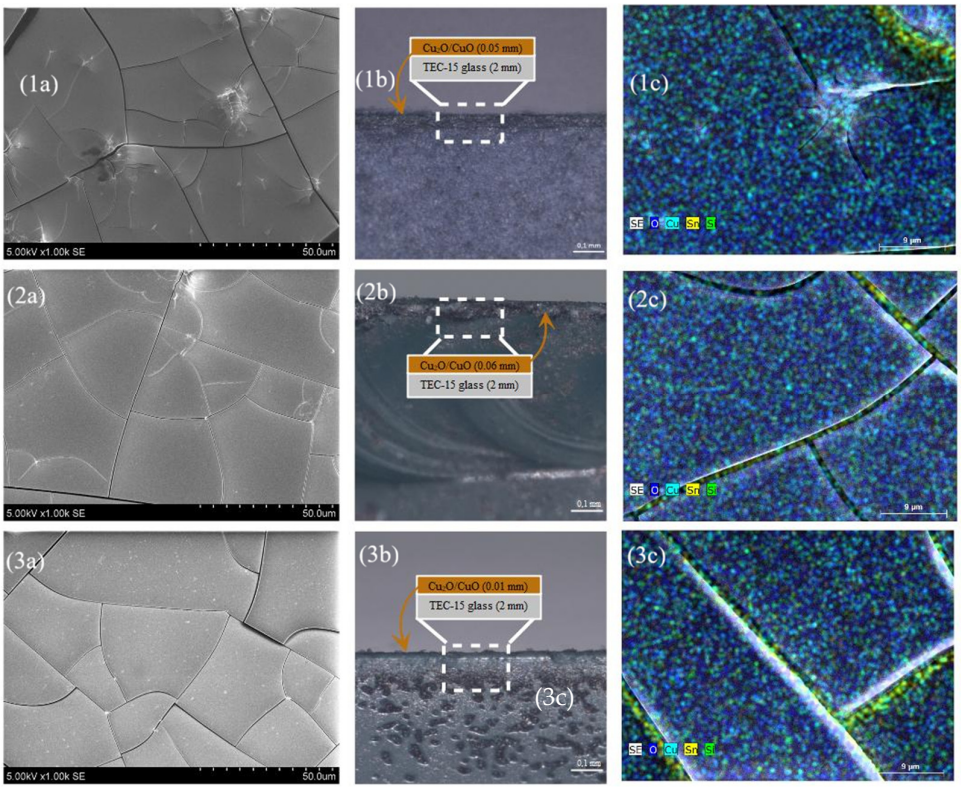

Figure 5. Morphological and elemental characterization of mixed-phase copper oxide coatings deposited at varying EPD voltages. SEM micrographs at (**1a**–**3a**) x1,000 magnification illustrating the primary film topography and characteristic mud-crack morphology; (**1b**–**3b**) cross layer thickness within a magnification range of 12× to 150×; and (**1c**–**3c**) Energy-dispersive X-ray spectroscopy (EDS) spectra confirming the elemental composition and quantitative reduction in copper loading as voltage increases for the (1) 0.9 V, (2) 1.0 V, and (3) 1.2 V catalysts.

EDS analysis in Figure 5(1c–3c) shows a substantial reduction in copper loading as the deposition voltage increases, with the 0.9 V coating containing 25.33 wt.% Cu compared to 15.25 wt.% for the 1.2 V sample. This chemical trend is accompanied by a relative increase in substrate-derived signals, such as Sodium (reaching 11.18%), suggesting greater electron beam penetration through the leaner high-voltage layers. These quantitative results chemically validate that lower EPD voltages achieve catalyst immobilization and a more robust material volume.

3.1.5. XRD Analysis of Copper Oxide Coatings After EPD

Following electrophoretic deposition, X-ray diffraction (XRD) examination was performed to determine the structural integrity and phase composition of the copper oxide coatings. The deposited films' diffraction patterns retained the distinctive reflections associated with mixed copper oxide phases, indicating that the EPD technique did not cause

significant phase transformation or crystallographic deterioration. The dominating peaks for the Cu_2O and CuO phases remained clearly visible, showing that the non-calcined character of the synthesized copper oxides was maintained throughout deposition. No additional crystalline phases associated with copper hydroxides or metallic copper were found within the instrument's resolution limitations, indicating satisfactory phase stability throughout deposition.

The copper oxide film deposited at 0.9 V exhibited 8 distinct XRD peaks with 2θ positions at 26.618°, 33.863°, 37.869°, 42.862°, 51.598°, 54.672°, 61.610°, and 65.626°.corresponding to d-spacing values ranging from 3.35 Å to 1.09 Å. Phase identification revealed a mixed Cu_2O/CuO structure, with the strongest reflection at 37.869° (18.90 Cps) corresponding to the principal CuO tenorite (111) reflection (JCPDS 05-0661) and the peak at 33.863° (8.91 Cps) matching CuO tenorite (111) plane and 65.626° to overlapping (220)/(311) planes (JCPDS 48-1548) [40,41]. Cu_2O reflections were identified at 42.862° corresponding to the (200) plane, and 61.610° to the (220) plane, all consistent with the cubic cuprite structure (JCPDS 05-0667) [45,46]. Crystallite sizes calculated using the Scherrer equation ranged from 10.9 nm to 62.4 nm, with an average of 30.9 nm, indicating good crystallinity with FWHM values between 0.136° and 0.445° [43,47]. This voltage condition demonstrates retention of mixed-phase composition with balanced Cu_2O/CuO coexistence, consistent with electrodeposition studies showing that lower overpotentials favor preservation of multiple copper oxide phases without aggressive electrochemical transformation [48,49].

At 1.0 V deposition voltage, the XRD pattern displayed eight peaks at 26.642°, 33.902°, 37.895°, 42.867°, 51.634°, 54.531°, 61.716°, and 65.635°. The dominant peak at 37.895° (19.20 Cps, S/N ratio 6.5) represents the strongest CuO tenorite (111) reflection (JCPDS 05-0661) among all voltage conditions, indicating optimized Cu_2O phase transfer and crystallization [31,40]. Peaks at 33.902° correspond to CuO tenorite ($\bar{1}11$) (JCPDS 48-1548), while 42.867° matches Cu_2O (200), 51.634° represents CuO (020) reflections, and 61.716° corresponds to Cu_2O (220)/(311) planes, suggesting a mixed-phase composition [26,45,50,51]. Crystallite sizes exhibited extreme variation from 8.6 nm to 99.0 nm, with an average of 30.6 nm, where the exceptionally large 99.0 nm crystallite at 74.723° (FWHM 0.112°) suggests in situ crystal growth or recrystallization during deposition [38,46]. This voltage condition demonstrates selective phase transfer with preferential Cu_2O enrichment (57% transfer efficiency for Cu_2O phases versus 22% for CuO phases from the T25 source), attributed to the lower density (6.0 g/cm^3 for Cu_2O vs. 6.3 g/cm^3 for CuO) and electrophoretic mobility of Cu_2O particles under intermediate electric field strength [43,47,52].

The 1.2 V deposition produced the most simplified XRD pattern with only eight peaks at 26.655°, 33.858°, 37.900°, 42.857°, 51.648°, 61.775°, and 65.629°, representing the most selective phase transfer among all conditions. Phase analysis identified a CuO structure with the strongest reflection at 37.900° (16.74 Cps) corresponding to CuO tenorite (111) (JCPDS 05-0661) and supporting peaks at 42.857° (Cu_2O (200)), 51.648° (CuO (020)), and 61.775° (Cu_2O (220)/(311)), alongside minor CuO contributions at 33.858° (tenorite ($\bar{1}11$), JCPDS 48-1548) and 65.629° ° [31,50,52]. Crystallite sizes were significantly reduced compared to lower voltages, ranging from 7.4 nm to 26.7 nm with an average of 19.4 nm and a narrower distribution, indicating that high voltage drives rapid nucleation density and kinetically limits crystal growth [43,47,53]. The complete absence of sub-stoichiometric reflections demonstrates an aggressive influence on the relative phase composition and deposition behavior of the deposited coatings, where the high electric field (1.2 V) suppresses metastable intermediates and preferentially deposits small, highly charged Cu_2O nanoparticles, consistent with electrodeposition literature showing that increased overpotentials favor higher nucleation rates over growth, producing finer-grained, more defect-rich crystallites [46,48,54].

Comparative analysis of the T25 copper oxide aging suspension (19 XRD peaks) with the deposited films reveals voltage-dependent selective phase transfer rather than simple physical particle deposition. The T25 source material exhibited a balanced mixed-phase distribution with Cu_2O peaks at 29.54° (Cu_2O (110), JCPDS 05-0667), 40.36° (Cu_2O (111)), 41.47° (Cu_2O (111)), 42.64° (Cu_2O (200)), 61.60° (Cu_2O (220)), and 75.17° (Cu_2O (311)) and CuO peaks at 32.04° (CuO (110), JCPDS 48-1548), 32.46° (CuO (002)/ ($\bar{1}$11)), 35.73° (CuO (111)), 38.81° (CuO (111)), 48.04° (CuO (020)), 58.34° (CuO (202)), 66.37° (CuO (113)/(220)), and 68.20° (CuO (220)) [29,41,42]. Four copper hydroxide peaks where found at 16.71° ($Cu(OH)_2$ (020)), 22.94° ($Cu(OH)_2$ (021)), 33.54° ($Cu(OH)_2$ (002)), and 35.64° ($Cu(OH)_2$ (111)). Only 6–8 of these peaks (32%–42% fidelity) were transferred to the glass substrates, with systematic 0.3–0.5° peak shifts indicating lattice parameter changes during deposition [15]. The selective phase transfer is evidenced in Figure 6, where the 0.9 V film maintains the highest fidelity to the T25 source and shows preservation of multiple Cu_2O and CuO reflections, demonstrating that low electric field strength allows gentle electrophoretic migration that maintains much of the source material's structural heterogeneity without significant electrochemical transformation [48,49,55]. In contrast, 1.0 V and 1.2 V conditions showed selective enrichment of specific phases, attributed to voltage-induced dissolution-redeposition mechanisms and electrochemical redox reactions at particle–electrolyte–electrode interfaces that purify the deposited phases [46,56,57].

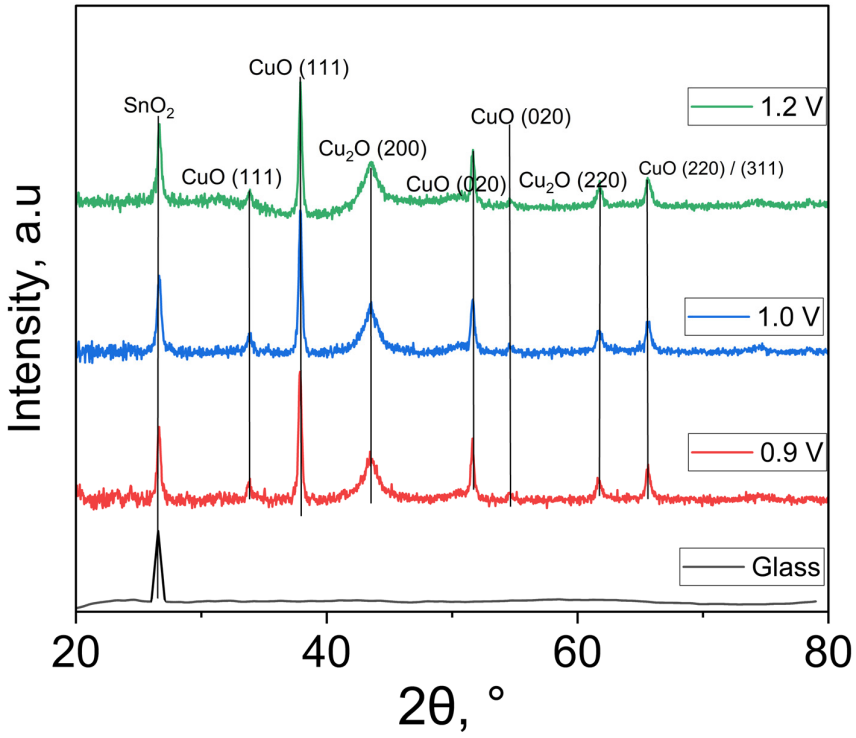

Figure 6. XRD Patterns of coatings at varying deposition voltages (0.9 V–1.2 V). Phase identification is indexed to JCPDS 05-0661 (CuO) and JCPDS 05-0667 (Cu_2O), showing the transition from a metastable multi-phase composite to a consolidated oxide structure.

The voltage-dependent phase transformation during EPD demonstrates that Cu_2O phases from the T25 source transfer 2.6 times more efficiently (57%) than CuO phases (22%) across all voltages, driven by Cu_2O's lower density (6.0 g/cm^3 vs. 6.3 g/cm^3 for CuO), colloidal stability, and favorable surface charge characteristics under applied electric fields [51,55,56]. From Table 1, at 0.9 V, the broad-spectrum transfer mechanism preserved the highest mixed-phase content with Cu_2O/CuO coexistence and crystallite sizes (10.9–62.4 nm) closely resembling the T25 source, making this voltage optimal for applica-

tions requiring extensive Cu_2O/CuO heterojunction interfaces for photocatalytic charge separation [29,34]. However, 1.0 V produced the highest quality mixed phase through selective Cu_2O enrichment combined with controlled CuO retention, evidenced by the strongest Cu_2O (200) reflection (19.20 Cps, JCPDS 05-0667), largest crystallite (99.0 nm), and emergence of new crystalline phases (54.531°, 74.716°), indicating in situ crystallization that enhances both phase purity and interfacial quality [31,52,58]. The 1.2 V condition, while producing the smallest crystallites (19.4 nm average) for maximum surface area, exhibited the lowest phase diversity with more crystalline Cu_2O phase peaks and minimal CuO contribution (33.858° reflection only), making it less suitable for heterojunction-dependent photocatalysis [34,53,54]. Therefore, 1.0 V represents the optimal voltage for producing high-quality mixed-phase Cu_2O/CuO films, balancing T25 phase transfer with enhanced crystallinity and controlled phase transformation that eliminates metastable intermediates while preserving critical Cu_2O/CuO interfaces necessary for efficient photocatalytic antibiotic degradation.

Table 1. Structural parameters and phase composition of precursor and EPD films.

Sample	Peaks	Phase Composition	Crystallite Size (nm)	Key Finding
T25	19	Highest mixed Cu_2O/CuO	25–35 (est.)	Best source material
T35	13	CuO-dominated	30–40 (est.)	Over-aged
0.9 V	8	Mixed Cu_2O/CuO	10.9–62.4 (avg 30.9)	High phase fidelity
1.0 V	8	Cu_2O-enriched	8.6–99.0 (avg 30.6)	Largest crystallite
1.2 V	8	Cu_2O-enriched relative to other voltages	7.4–26.7 (avg 19.4)	Smallest nanocrystals

3.1.6. Optical Properties and Band Gap Analysis

The optical properties of the electrodeposited coatings were evaluated via UV–Vis diffuse reflectance spectroscopy, revealing characteristic absorption edges between 550 nm and 700 nm. The optical characterization was performed to evaluate visible-light absorption properties, while the photocatalytic experiments reported in this study were conducted under UV irradiation as a controlled evaluation of catalytic performance. Following the Kubelka–Munk transformation of raw reflectance data and subsequent Tauc plot extrapolation for direct allowed transitions, the optical band gaps (Eg) were determined to be 1.90 eV (0.9 V), 2.04 eV (1.0 V), and 2.0 eV (1.2 V) as seen in Figure 7. This systematic blue shift suggests that the applied EPD voltage influences the relative phase composition, crystallinity, and structure of the deposited coatings; higher voltages (1.0 V) aggressively stabilize the wider-gap Cu_2O phase (~2.1 eV), whereas the 0.9 V "Marathon" catalyst maintains a balanced CuO/Cu_2O heterojunction with a narrower gap (1.90 eV) optimized for harvesting a broader solar spectrum. The observed blue shift may arise from changes in phase composition, crystallinity and defect concentration.

The reflectance spectrum supports this disparity, as the 1.2 V coating reflects significantly more low-energy visible light (e.g., ~29.7% at 650 nm) compared to the 0.9 V film (~15.9% at 650 nm), proving the 0.9 V film's enhanced capacity to absorb the photons required for the 18% TOC removal achieved in real wastewater. This suggests that EPD voltage acts as a precision electronic engineering tool for tuning the band gap of these semiconductor heterojunctions. Based on the identified CuO/Cu_2O mixed-phase composition, optical properties, and HPLC–MS analysis of CIP transformation products, a proposed mechanism is illustrated in Figure 8.

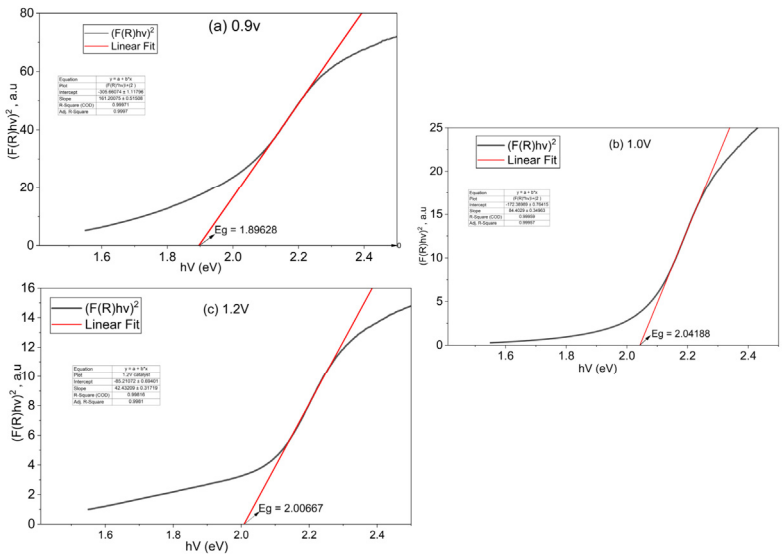

Figure 7. Tauc plots of various copper catalysts.

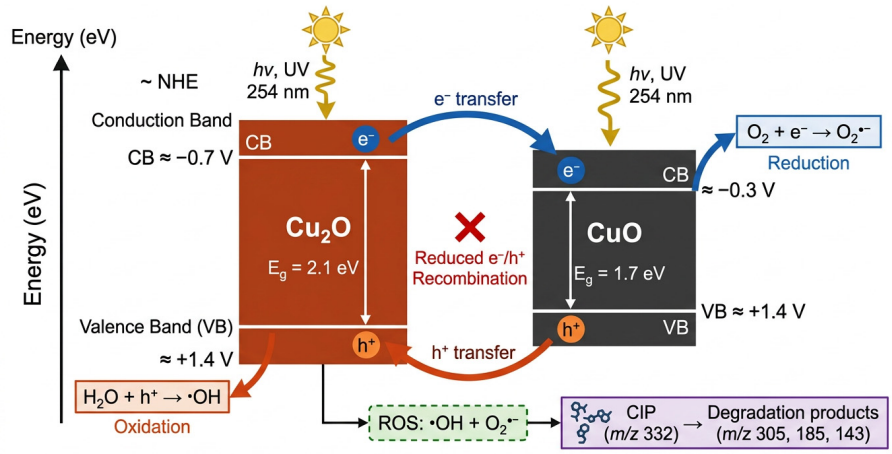

Figure 8. Proposed photocatalytic mechanism of the CuO/Cu_2O mixed-phase coating under irradiation (Band alignment adapted from literature; not drawn to exact scale).

3.2. Evaluation of Photocatalytic Performance and Pollutant Remediation Mechanisms

3.2.1. Methylene Blue Photocatalysis

Photocatalytic experiments were conducted using glass-supported copper oxide coatings to establish the intrinsic activity of the deposited films and to optimize the electrophoretic deposition (EPD) voltage under controlled conditions. Methylene blue (MB) was utilized as a model organic pollutant to establish the intrinsic photocatalytic activity of the electrodeposited films and to determine the optimal deposition parameters. Preliminary results indicated that a 10 min deposition time provides the most favorable balance of catalyst loading and light penetration; shorter durations resulted in insufficient surface coverage, while deposition times exceeding 10 min led to excessive film thickness, which triggered light-shielding effects and hindered mass transfer.

The 30 min degradation kinetics of MB revealed in Figure 9 shows a potential-dependent hierarchy that correlates with the preserved phase diversity of the coatings. As shown in the performance profiles, the 1.0 V catalyst achieved the highest overall degradation, reaching a C/C_0 ratio of approximately 0.94, followed closely by the 0.9 V film. Although the 1.2 V catalyst demonstrated a more aggressive degradation rate between the 10 and 15 min marks, its activity plateaued significantly toward the end of

the cycle, ultimately resulting in a higher residual concentration compared to the lower-voltage films. The degradation follows pseudo-first-order kinetics where the 1.0 V catalyst achieved the highest activity (k_{app} = 0.0017 min^{-1}), demonstrating that the mixed-phase catalyst preserved at lower voltages provides more sustained charge separation than more phase-pure structures.

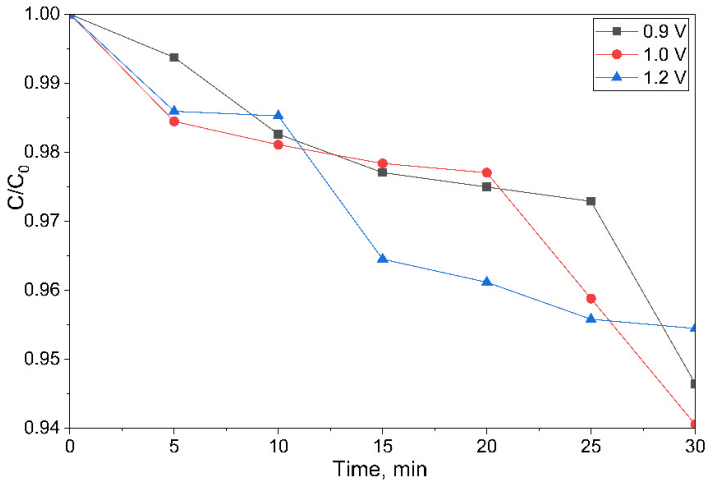

Figure 9. Methylene blue degradation.

3.2.2. CIP Adsorption Kinetics and Phase Composition Effects

Prior to photocatalytic degradation of ciprofloxacin, dark adsorption experiments were performed to evaluate the affinity of the coatings toward the antibiotic and to establish comparable adsorption conditions among samples. The ciprofloxacin adsorption kinetics over 30 min in Figure 10 revealed a counterintuitive trend where the 0.9 V film achieved the highest removal efficiency (13.5%), followed by 1.0 V (11.0%), and 1.2 V (7.5%), despite the 1.2 V film possessing the smallest crystallite size (19.4 nm average) and presumably the highest specific surface area. This performance hierarchy directly correlates with the voltage-dependent phase evolution characterized by XRD, where the 0.9 V film's highest degree of mixed Cu_2O/CuO phase coexistence (balanced cuprite (200) at 42.862° and tenorite ($\bar{1}11$) at 33.863°) provides diverse binding interactions including electrostatic attraction, hydrogen bonding, and π–π interactions that enhance ciprofloxacin uptake [59,60]. The literature suggests that mixed CuO/Cu_2O composites outperform phase-pure materials in antibiotic remediation through complementary surface chemistries, with studies demonstrating that heterojunction interfaces create a broader spectrum of high-affinity adsorption sites compared to single-phase surfaces [59–61]. The 1.0 V film's intermediate performance reflects its Cu_2O-enriched composition (strongest (200) reflection at 42.862°) with controlled CuO retention, while the 1.2 V film's Cu_2O dominance and minimal CuO contribution (weak ($\bar{1}11$) at 33.858° only) limit chemical diversity and reduce overall adsorption affinity despite its high surface area [55,56]. Ciprofloxacin adsorption follows a pseudo-second-order model, reaching equilibrium within 30–40 min, with the 0.9 V film achieving the highest efficiency of 13.5% due to its possibly enhanced phase diversity and diverse binding interactions. This performance hierarchy indicates that chemical affinity and electrostatic interactions at the CuO/Cu_2O interfaces override simple surface area advantages, as evidenced by the high R^2 of 0.96 for the 1.0 V catalyst versus the poor fit for the 1.2 V film. Ciprofloxacin adsorption kinetics were rigorously evaluated and confirmed to follow a first-order model, with R^2 values of 0.89 (0.9 V), 0.96 (1.0 V), and 0.9 (1.2 V). The 0.9 V film achieved a superior removal efficiency of 13.5%, driven by its enhanced phase diversity and multifaceted binding interactions. This performance

hierarchy proves that chemical affinity and electrostatic interactions at the CuO/Cu_2O heterojunction interfaces override simple surface area advantages, as evidenced by the strong R^2 correlation for the 1.0 V catalyst which validates a consistent and efficient mass transfer mechanism.

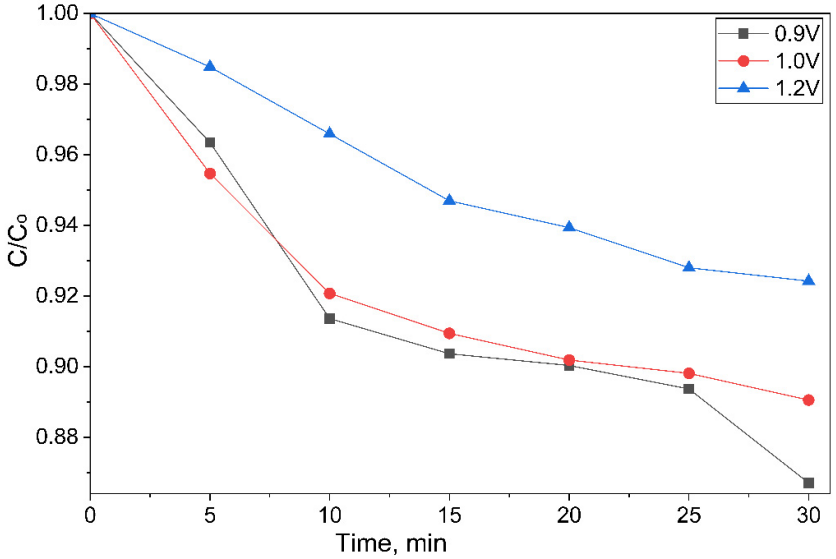

Figure 10. Ciprofloxacin adsorption kinetics (Dark Phase).

The observed adsorption behavior demonstrates that surface chemistry and phase composition dominate over crystallite size and surface area effects, as the smallest nanocrystals (1.2 V: 7.4–26.7 nm) exhibited the slowest kinetics while larger crystallites (0.9 V/1.0 V: ~30 nm average) demonstrated enhanced performance. This phenomenon is supported by literature showing that copper oxide materials with favorable surface zeta potentials can achieve markedly higher ciprofloxacin adsorption despite lower BET surface area, indicating that electrostatic interactions and chemical affinity override textural advantages [62,63]. The rapid initial adsorption within the first 5 min (3.6%–4.5% removal for 0.9 V/1.0 V versus 1.4% for 1.2 V) followed by a slower approach to equilibrium is consistent with pseudo-second-order kinetics commonly reported for ciprofloxacin uptake on copper oxide photocatalysts, with typical equilibrium times of 30–40 min [60,64,65]. The steeper initial slope for mixed-phase films (0.9 V/1.0 V) reflects higher adsorption rate constants and more favorable thermodynamic driving forces arising from Cu_2O/CuO heterojunction interfaces, grain boundaries, and surface heterogeneity that create high-energy reactive sites for ciprofloxacin binding [59,61,63]. Therefore, the 0.9 V EPD condition produces the optimal adsorbent by preserving the mixed Cu_2O/CuO character of the T25 source material (42% peak fidelity), emphasizing that rational design of copper oxide photocatalysts for antibiotic adsorption requires balancing phase composition and surface chemistry rather than simply maximizing surface area through extreme nanosizing [59,60,62].

3.2.3. Photocatalytic Degradation Kinetics and Phase Composition Effects

The photocatalytic degradation of ciprofloxacin (CIP) over the electrodeposited copper oxide films follows a potential-dependent efficiency, as shown in the Cu_2O/CuO profiles. The control experiment showed minimal CIP degradation (<5% after 60 min), indicating that direct photolysis under the experimental conditions is negligible and that the observed degradation in the presence of copper oxide films is primarily due to photocatalytic processes. This finding is consistent with previous studies showing that CIP is relatively stable under UV–Visible irradiation in the absence of a photocatalyst [4,66]. In synthetic aqueous solutions (model water), the 0.9 V film proves in Figure 11 to be the ultimate

"marathon" performer, exhibiting the fastest overall kinetics and achieving near-complete removal of the antibiotic by the 50 min mark, while the 1.0 V and 1.2 V films show slower degradation rates, with 1.2 V retaining approximately 10% of the initial concentration after one hour. This performance hierarchy is governed by the nanocrystalline structure and phase composition; for instance, the 1.2 V film's smaller crystallite size (19.4 nm) provides a high density of active sites and a Cu_2O-enriched phase that enhances visible-light photosensitivity [67,68]. The nanocrystalline architecture ensures shorter carrier diffusion distances, allowing photogenerated reactive oxygen species (ROS) to efficiently reach the catalyst surface and initiate the oxidative destruction of the antibiotic [67,69].

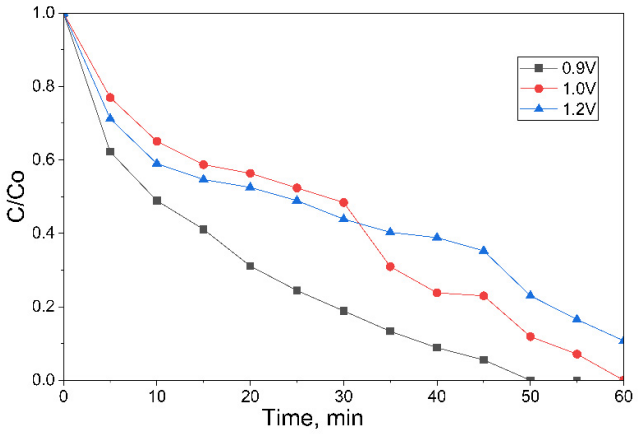

Figure 11. Photocatalytic degradation of CIP in synthetic aqueous solution.

The voltage-dependent performance also reflects differences in charge separation efficiency facilitated by Cu_2O/CuO heterojunctions. These interfaces suppress bulk recombination through possible heterojunction mechanisms, preserving high-energy electrons and holes for the mineralization of the quinolone structure [67,70]. While lower-voltage films (0.9 V and 1.0 V) possess larger crystallites (~30 nm) and demonstrate stronger initial adsorption, their photocatalytic conversion in the provided data suggests a more favorable band alignment or higher surface area that maximizes charge carrier utilization [67]. Ultimately, the Cu_2O-rich surfaces promote efficient light harvesting and ROS generation, ensuring the progressive fragmentation of ciprofloxacin into stable intermediates even within complex wastewater matrices [67,69,70].

The degradation kinetics were analyzed using both first-order and pseudo-first-order models:

$$\ln(C/C_0) = -k_{app} \cdot t$$

where k_{app} is the apparent rate constant.

The calculated rate constants were tabulated in Table 2: 0.9 V (0.059 min^{-1}, R^2 = 0.98) compared to R^2 =0.843 for first-order, first-order for 1.0 V (0.042 min^{-1}, R^2 = 0.96) compared to pseudo-first-order R^2 = 0.89, and first-order for 1.2 V (0.030 min^{-1}, R^2 = 0.90) compared to pseudo-first-order R^2 = 0.86. The higher rate constants for the 0.9 V and 1.0 V films support their better photocatalytic performance compared to the 1.2 V film. These results demonstrate that voltage-dependent phase transfer during EPD can be exploited to optimize photocatalytic activity by controlling the CuO/Cu_2O ratio and film microstructure.

Given these results, reusability and stability assessments are critical for identifying the most viable catalyst for practical wastewater treatment. The 1.0 V and 0.9 V films represent the most promising candidates due to their high removal efficiency and structural robustness. Specifically, the 1.0 V film offers a balanced compromise between photocatalytic activity and mechanical stability, supported by its significant grain growth (averaging

99.0 nm in specific regions) and optimized Cu_2O enrichment (noted by the (200) reflection at 42.862°). Such structural characteristics enhance resistance to photo-corrosion over multiple cycles, a common limitation in copper-based catalysts [66,68]. Standard reusability protocols typically verify that high-performance materials maintain over 85% of their initial activity after 4–6 cycles; thus, the 1.0 V film's controlled mixed-phase composition provides the necessary surface integrity for sustained performance in long-term applications [66,67].

Table 2. Comparison of kinetic model fitting parameters (R^2) for CIP photodegradation and adsorption over CuO/Cu_2O coatings at different deposition voltages.

Catalyst	First-Order R^2	Pseudo-First-Order R^2	Adsorption R^2
0.9 V	0.843	**0.980**	0.890
1.0 V	**0.966**	0.890	**0.960**
1.2 V	0.900	0.860	0.900

Bold numbers indicate the best fitting models for the preferred catalyst.

3.2.4. Evaluation of Photocatalytic Reusability and Structural Stability

The long-term stability and reusability of the synthesized films were evaluated over five consecutive 60 min cycles to assess their practical potential for continuous wastewater treatment. Figure 12 demonstrates the exceptional stability of the 0.9 V catalyst compared to the progressive decline of the 1.2 V film. The 0.9 V catalyst demonstrated exceptional performance and structural robustness in Figure 12a, maintaining complete ciprofloxacin removal (C/C_0) throughout the entire 300 min testing period. In each of the five cycles, the parent compound was effectively eliminated within approximately 50 to 55 min, indicating that the mixed-phase CuO/Cu_2O heterojunction remains highly active and resistant to photo-corrosion or active site poisoning.

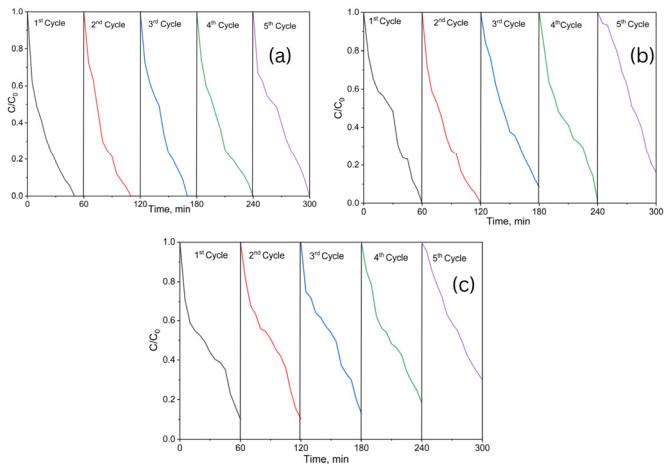

Figure 12. Reusability and stability profile of various catalysts over five consecutive cycles: (**a**) 0.9 V, (**b**) 1.0 V and (**c**) 1.2 V.

In contrast, Figure 12b shows that the higher-voltage catalysts exhibited a distinct and progressive loss of efficiency over repeated use. While the 1.0 V film initially achieved complete degradation, it showed the first signs of performance fluctuation in the third and fifth cycles, where a residual concentration of $C/C_0 \approx 0.10$ and 0.15 remained, respectively. The 1.2 V catalyst in Figure 12c proved to be the most unstable, failing to reach complete removal even in the first cycle ($C/C_0 \approx 0.1$) and displaying a significant, linear decline in activity that culminated in a 30% residual antibiotic concentration ($C/C_0 \approx 0.3$) by the conclusion of the fifth cycle.

This reusability trend reinforces the "sprint versus marathon" dynamic observed in earlier kinetics studies. While the phase-pure Cu_2O in the 1.2 V film may facilitate a rapid initial "sprint" in transformation, its smaller nanocrystalline domains and susceptibility to parasitic oxygen evolution reactions lead to a rapid exhaustion of catalytic activity. Conversely, the structural complexity and heterojunctions preserved in the 0.9 V and 1.0 V films provide the necessary stability for a sustained "marathon" performance, ensuring consistent water quality improvement over multiple remediation cycles without significant material degradation. Leaching remains safely below 1.2 mg/L, with 0.9 V maintaining perfect 5-cycle reusability and 1.2 V showing rising copper release and progressive activity loss.

Microscope measurements showed that lower voltages produced significantly bulkier coatings (0.9 V: 0.04–0.09 mm; 1.0 V: 0.06–0.07 mm) compared to the minimal 0.01 mm layer at 1.2 V. This increased catalyst loading in the 0.9 V mixed-phase film provides the structural reservoir necessary to maintain its perfect 5-cycle reusability.

3.2.5. Comparative Performance Analysis with Literature Analogs

To evaluate the competitive standing of the optimized 0.9 V mixed-phase catalyst, its performance parameters were benchmarked against recently reported CuO/Cu_2O heterojunctions synthesized through various high-energy methods (Table 3). Notably, our room-temperature co-precipitation and EPD strategy achieves a possibly enhanced apparent rate constant (k_{app} = 0.059 min^{-1}) compared to analogs requiring calcination at 300 °C or specialized microwave techniques. This comparison highlights that our phase composition and deposition behavior of the deposited coatings effectively preserve the synergistic CuO/Cu_2O interfaces necessary for sustained antibiotic degradation while offering a significantly more sustainable, low-energy fabrication pathway.

Table 3. Photocatalytic performance: Literature comparison.

Parameter	This Work	Tsai et al. [71]	Zhu et al. [72]	Kumar et al. [73]
Catalyst	Mixed-phase CuO/Cu_2O	Cu_xO/MOF	$CuO/Cu_2O/CuS/ZnO$	$Cu/Cu_2O/CuO$
Synthesis	Low-temp co-precip. + EPD	Calcination (300 °C)	Microwave technique	Wet chemical (RT)
Pollutant	Ciprofloxacin	Ciprofloxacin	Sulfamethoxazole	Congo red/Dyes
Efficiency	100% removal (60 min)	92% removal (120 min)	99.17% (60 min)	80% removal (120 min)
Rate	0.059 min^{-1}	0.048 min^{-1}	0.0380 min^{-1}	Not reported
Stability	5 Cycles (Stable)	>85% (6 cycles)	Not reported	Not reported

3.2.6. Analytical Identification of Intermediate Products for Synthetic Wastewater

The degradation behavior of ciprofloxacin was examined at three applied potentials (0.9, 1.0, and 1.2 V) over treatment times of 0, 5, and 10 min. In all cases, the initial samples (0 min) were dominated by the protonated molecular ion of ciprofloxacin at m/z = 332, indicating that the antibiotic remained structurally intact prior to treatment.

Figure 13a shows the HPLC–MS examination of the degradation of ciprofloxacin (CIP) utilizing a 0.9 V electrodeposited copper oxide catalyst. It displays a distinct time-dependent transformation mechanism, progressing from the intact molecular structure to smaller oxidative intermediates. At the initiation point (0 min), CIP is predominantly identified as the protonated molecular ion at m/z = 332, accompanied by characteristic fragment ions in the vicinity of m/z 314–315 [4], thereby corroborating the presence of the intact quinolone and piperazine moiety. Following a 5 min exposure, there is a marked reduction in the intensity of the parent ion, signifying the commencement of degradation, while novel intermediate species appear, especially at m/z = 305, alongside persistent

ions around m/z 329–330, consistent with initial piperazine ring cleavage and partial defluorination. Simultaneously, an increase in lower molecular weight fragments such as m/z 143, 169, and 185 signifies the progressive degradation of the quinolone core structure. By the 10 min mark, the degradation process progresses further, characterized by the continued attenuation of the parent peak and the prominence of intermediate and low-mass fragments, suggesting extensive structural fragmentation through sequential oxidative reactions, including oxidation, deamination, and ring opening. Nevertheless, the sustained presence of intermediate ions, particularly within the m/z 315–330 range, indicates that complete mineralization is not realized under the examined conditions, with the degradation process being predominantly governed by partial oxidation pathways that lead to stable intermediate products, rather than achieving full conversion to CO_2 and H_2O.

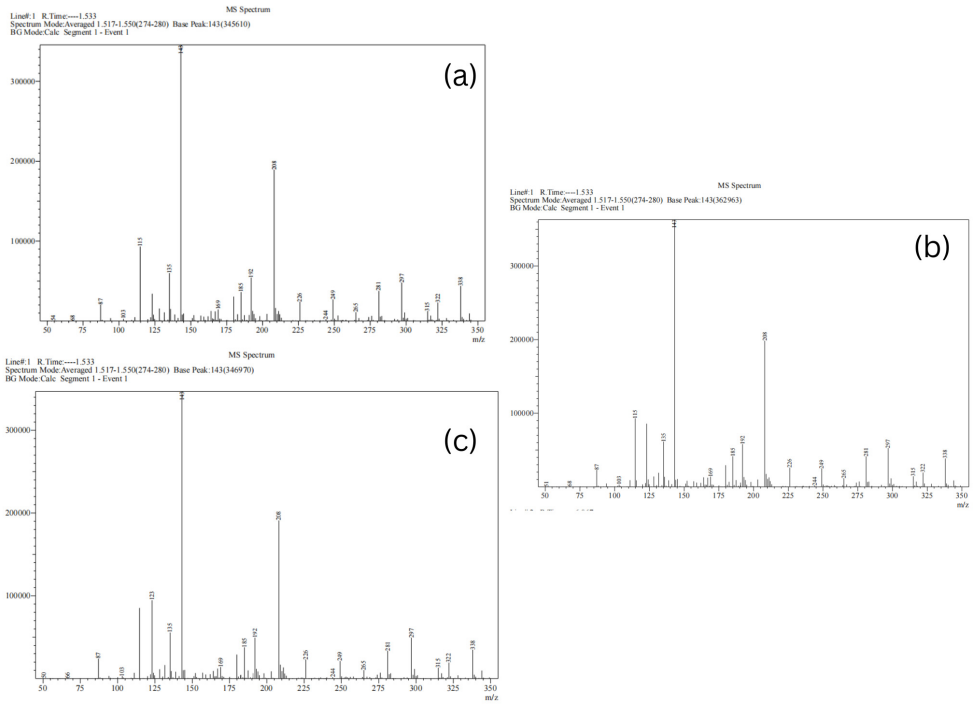

Figure 13. HPLC profile of different catalysts for synthetic wastewater degradation: (**a**) 0.9 V, (**b**) 1.0 V and (**c**) 1.2 V.

The HPLC–MS analysis in Figure 13b for the 1.0 V electrodeposited catalyst reveals a degradation pattern slightly more pronounced than the lower-voltage conditions. While the untreated 0 min sample is dominated by the intact protonated molecular ion of ciprofloxacin at m/z = 332, a 5 min treatment interval leads to the emergence of intermediate species at m/z 329–331 and 315. By the 10 min mark, the relative intensity of these transformation products increases significantly, accompanied by the appearance of small fragments at m/z 143 and 123. The specific MS spectrum for this condition identifies m/z 143 as the base peak, which represents an advanced oxidation stage in the degradation process. Other prominent signals such as m/z 208, 192, and 185 [4] corroborate the progressive oxidative modification and fragmentation of the antibiotic's quinolone core.

At the highest applied potential of 1.2 V, the ciprofloxacin molecule undergoes the most extensive structural transformation within the 10 min observation window. Following treatment, Figure 13c reveals that there is a substantial decrease in the parent ion's intensity, signaling rapid degradation into multiple prominent transformation products. These include early-stage intermediates at m/z 329–331 and 315 [4,74], as well as secondary

fragments like m/z 123 and 143. The MS spectrum for the 1.2 V film suggests m/z 143 as the base peak, indicating a deep degradation stage through piperazine ring cleavage and core destruction. Despite this aggressive fragmentation, the continued presence of intermediate ions suggests that the pathway is dominated by partial oxidation rather than full mineralization to CO_2 and H_2O.

The observed fragmentation pattern, particularly the formation of ions at $m/z \approx 329$, 305, 185, and 143, is in strong agreement with previously reported Cu-assisted advanced oxidation pathways, suggesting that ciprofloxacin degradation proceeds via piperazine ring cleavage, defluorination, and progressive quinolone core destruction rather than direct mineralization. The enhanced photocatalytic activity of the mixed-phase CuO/Cu_2O coatings can be attributed to the synergistic interaction between the two semiconductor phases. Under irradiation, photoexcited electrons and holes are generated within the copper oxide structure. The presence of CuO/Cu_2O heterojunction interfaces promotes charge separation and suppresses electron–hole recombination, thereby increasing the lifetime of reactive charge carriers. These charge carriers react with dissolved oxygen and water to generate reactive oxygen species, including superoxide ($\cdot O_2^-$) and hydroxyl ($\cdot OH$) radicals, which are responsible for the oxidative degradation of ciprofloxacin and its subsequent transformation into lower-molecular-weight intermediates.

Overall, the results demonstrate a clear time-dependent degradation trend across all potentials, where increasing treatment time from 0 to 10 min promotes the gradual transformation of ciprofloxacin from the parent molecule into intermediate oxidation products and smaller fragments as summarized in Table 4.

Table 4. Proposed ciprofloxacin degradation pathway over Cu_xO catalysts (HPLC–MS assignment).

m/z	Assigned Species/Transformation	Reaction Type	Interpretation in Your System	References
332	Parent ciprofloxacin (CIP)	—	Intact molecule (baseline, 0 min)	
329	Defluorinated/hydroxylated CIP	Defluorination/hydroxylation	Intermediate oxidation stage	[75]
315	Oxidative intermediate	Oxidation	Early oxidation of quinolone core	[75]
305	Piperazine ring cleavage product	Dealkylation/ring cleavage	First major degradation step	[76]
285–290	Further degraded quinolone fragments	Ring opening	Loss of structural integrity	[74,77]
169–185	Ring-opened aromatic intermediate	Ring cleavage	Breakdown of quinolone backbone	
143	Small aromatic amine intermediate	Advanced oxidation	Deep degradation stage	
<120	Low molecular weight species	Mineralization intermediates	Approach toward CO_2/H_2O (incomplete)	

3.2.7. Analyzing TOC Removal Efficiency

Figure 14 illustrates the Total Organic Carbon (TOC) removal from a real wastewater matrix spiked with 10 mg/L of ciprofloxacin over a 60 min electrochemical treatment period using the various electrodeposited catalysts. We used 10 mg/L CIP in TOC analysis to ensure a clear signal-to-noise ratio against the background organic matter in real wastewater.

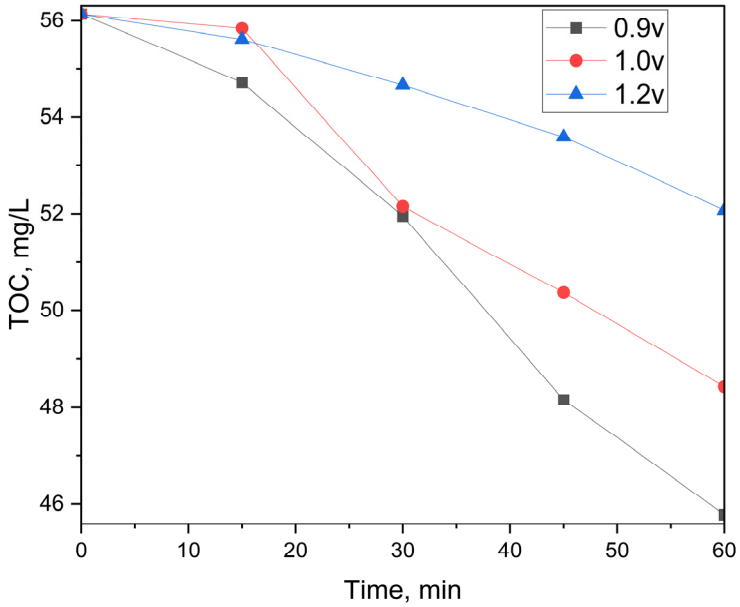

Figure 14. Total Organic Carbon (TOC) removal in real wastewater matrix.

Starting from an initial TOC concentration of approximately 56 mg/L, Figure 14 reveals a clear potential-dependent mineralization trend where the lowest applied potential of 0.9 V surprisingly yields the highest removal efficiency, reducing the TOC to roughly 46 mg/L (an ~18% reduction). In contrast, the 1.0 V and 1.2 V treatments resulted in higher residual TOC levels of approximately 48.5 mg/L and 52 mg/L, respectively. This behavior suggests that in a complex real wastewater matrix, lower potentials may favor more selective oxidation pathways or maintain better catalyst stability, whereas higher potentials (1.2 V) might be hampered by parasitic reactions like the oxygen evolution reaction (OER), which competes with the degradation of organic matter [67,78]. While the ciprofloxacin molecule itself undergoes significant structural transformation as evidenced by the fragmentation into lower m/z species, the relatively modest overall TOC reduction indicates that the process leads to the formation of stable organic intermediates rather than complete mineralization to CO_2 and H_2O under these specific conditions [66,68].

3.2.8. Evaluation of Ciprofloxacin Transformation Pathways in Real Wastewater Effluents

The photocatalytic remediation of ciprofloxacin (CIP) in a complex, biologically and chemically treated wastewater matrix was evaluated using HPLC–MS to monitor the persistence of the parent compound and the emergence of transformation products (TPs) over a 60 min duration. The original wastewater matrix exhibits a complex background of dissolved effluent organic matter (dEfOM), characterized by persistent ions at m/z 143, 252, 329, and 419. Upon spiking with CIP, the initial sample (0 min) is dominated by the protonated molecular ion at m/z 332 with a chromatographic intensity of 97.878 mAU at RT 4.849 min.

1. Initial Transformation Kinetics (0–15 min)

Within the first 5 min of treatment, a potential-dependent "sprint" is observed in Figure 15 where the 1.2 V catalyst demonstrates the highest efficiency in transforming the parent molecule, reducing the CIP peak intensity to 50.638 mAU, compared to 54.267 mAU for 1.0 V and 55.732 mAU for 0.9 V. This rapid transformation is accompanied by the primary cleavage of the piperazine ring, evidenced by the emergence of the m/z 305 fragment. By the 15 min mark, the hierarchy begins to shift; the 1.0 V catalyst achieves a

more significant reduction in the parent peak (39.956 mAU) compared to the 1.2 V catalyst (45.616 mAU), while the 0.9 V system reaches 42.256 mAU.

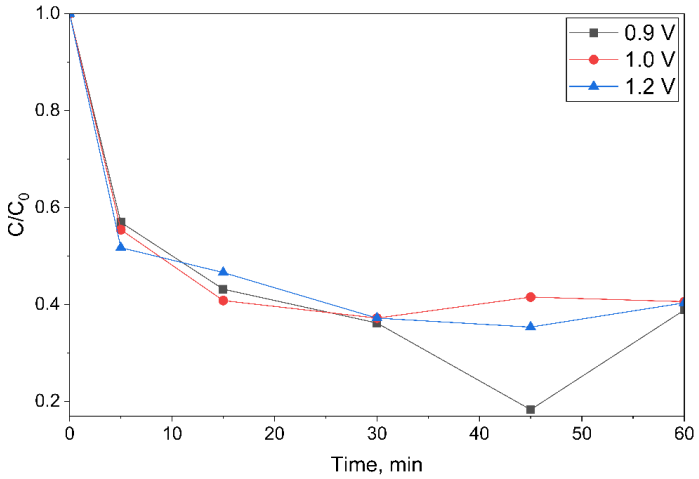

Figure 15. HPLC transformation profiles in wastewater (sprint vs. marathon).

2. Intermediate Proliferation and Core Opening (30 min)

At the 30 min interval, the three catalytic systems exhibit comparable levels of parent compound attenuation, with intensities plateauing around 35–36 mAU. During this phase, the degradation pathway advances from simple substituent removal to the oxidative opening of the quinolone core. This is marked by the prominence of the m/z 245 intermediate, alongside stable fragments at m/z 316 and 331. The persistence of these intermediates across all voltages at this stage suggests that while the antibiotic's biological activity is likely neutralized through structural modification, the resulting organic fragments are resistant to immediate mineralization.

3. Advanced Fragmentation and Long-Term Superiority (45–60 min)

In the final stages of treatment (45–60 min), the 0.9 V catalyst emerges as the most effective for advanced long-term degradation. At 45 min, the 0.9 V system reduces the parent CIP peak to its lowest recorded intensity of 17.930 mAU, significantly outperforming the 1.2 V (34.594 mAU) and 1.0 V (40.659 mAU) catalysts. By 60 min, the chromatographic profile reflects a deep structural destruction of the antibiotic; while the residual parent peak intensities are similar across the systems (~38–39 mAU), the 0.9 V catalyst produces a significantly more intense TP peak at RT 5.50 min (45.263 mAU) compared to the 1.2 V system (26.706 mAU), indicating a more thorough conversion of the initial molecule into advanced fragments.

Following 60 min of photocatalytic treatment in the wastewater matrix, the percentage of residual ciprofloxacin remaining relative to the initial 97.878 mAU signal is 38.88% for the 0.9 V catalyst, 40.59% for the 1.0 V catalyst, and 40.34% for the 1.2 V catalyst.

3.2.9. Proposed Mechanistic Pathway

The integrated HPLC–MS data suggest that ciprofloxacin degradation in real wastewater, as seen in Figure 16, follows an oxidative pathway initiated by piperazine ring cleavage (m/z 305) [76] and an oxidative intermediate (m/z 314–315) [75]. This is followed by defluorination and hydroxylation (m/z 329–330) and the formation of lower-molecular-weight quinolone-derived intermediates (m/z 245). The final 60 min status is characterized by a high intensity of small aromatic and amine fragments, specifically the m/z 143 ion, which becomes a dominant feature in all TIC(+) spectra. Ultimately, the mixed-phase CuO/Cu_2O

heterojunction preserved in the 0.9 V and 1.0 V films facilitates deeper fragmentation than the phase-pure 1.2 V film, which is limited by parasitic oxygen evolution reactions in the complex wastewater environment.

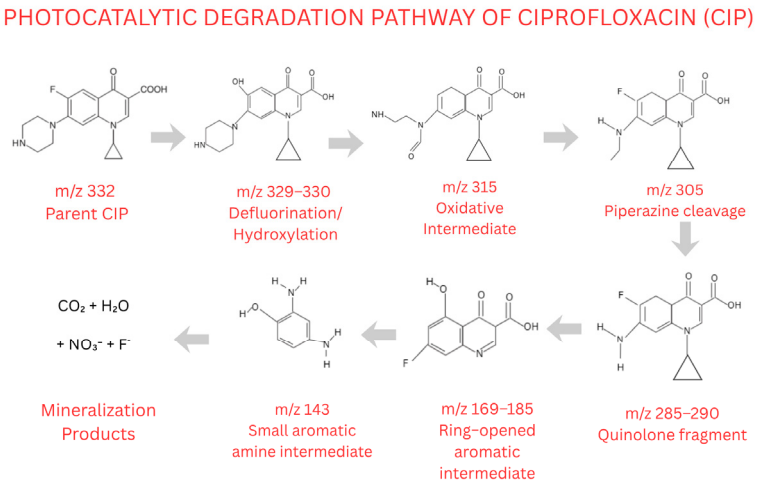

Figure 16. Proposed ciprofloxacin degradation pathway over Cu_xO catalysts.

Ultimately, the consistent emergence of transformation products such as m/z 288 [79] and 316 [4] across all applied potentials supports a shared oxidative pathway. This mechanism remains highly functional even in the presence of persistent wastewater background ions (e.g., m/z 143, 252, and 329), which characterize the biologically and chemically treated effluent. Among the tested conditions, the 1.0 V film provides the most robust compromise for practical remediation, balancing advanced initial catalytic activity with the long-term structural stability and grain growth (averaging 99.0 nm) required to resist photo-corrosion during repeated use.

The integrated findings reveal that the structural heterogeneity and metastable phases preserved in the T25 precursor (aged 25 min) are successfully transferred to glass substrates via low-voltage EPD. Specifically, the 0.9 V and 1.0 V films maintain the critical CuO/Cu_2O heterojunctions necessary for effective pollutant adsorption and mineralization. While the 1.2 V catalyst demonstrated the most rapid initial transformation of ciprofloxacin within a complex wastewater matrix, reducing the chromatographic signal to 50.6 mAU after five minutes, it was ultimately less effective for sustained remediation. Conversely, the 0.9 V catalyst consistently outperformed higher-voltage counterparts in deep cleaning, achieving a 13.5% adsorption efficiency and 18% Total Organic Carbon (TOC) removal. This hierarchy proves that phase diversity and favorable surface chemistry override the simple surface area advantages typically associated with smaller nanocrystals.

Table 5 highlights the "counterintuitive" finding that surface chemistry (mixed phases) is more important than surface area (crystallite size) for this system.

Table 5. Comparative adsorption and photocatalytic performance.

Catalyst	CIP Adsorption (30 min)	Photocatalytic Degradation (60 min)	TOC Removal (60 min)	Performance Driver
0.9 V Film	13.5%	~100% (50 min) (model water)	18%	Maximum interface area.
1.0 V Film	11.0%	High	~13%	Balanced activity and mechanical stability.
1.2 V Film	7.5%	~90%	~7%	High surface area but limited by phase purity.

3.3. Future Directions

While this study establishes the effectiveness of low-temperature synthesized CuO/Cu_2O heterojunctions for the rapid transformation of ciprofloxacin, several avenues remain for further investigation to enhance the practical viability of this technology:

1. Enhancement of Mineralization Efficiency: The relatively modest Total Organic Carbon (TOC) reduction (maximum 18% for the 0.9 V catalyst) suggests that while the parent antibiotic is fragmented, the process primarily leads to stable organic intermediates rather than full conversion to CO_2 and H_2O. Future work should focus on optimizing irradiation times beyond 60 min and exploring dual-catalyst systems or auxiliary oxidants (such as H_2O_2, ozone or persulfate) to drive the mineralization of persistent low-molecular-weight fragments like m/z 143 and 123.
2. Toxicity and Persistence of Transformation Products: HPLC-MS analysis identified a significant population of intermediates in the m/z 288–388 range. Although the parent ciprofloxacin is removed, the "cleanliness" of the final water must be verified through ecotoxicity assays (e.g., Vibrio fischeri or algal growth inhibition tests) to ensure that the formed transformation products do not retain antimicrobial activity or possess higher toxicity than the original compound.
3. Precision Heterojunction Engineering: The findings highlight that a 25 min precursor aging time (T25) is essential for preserving the metastable mixed-phase character. Further research could investigate the use of doping agents (e.g., Fe, Zn, or Ni) or the construction of ternary composites to further improve visible-light harvesting and interfacial charge separation, potentially overcoming the parasitic oxygen evolution reactions observed at higher deposition voltages.
4. Matrix Interferences and Scale-Up: This study successfully demonstrated performance in a complex, biologically treated wastewater matrix. Future studies should evaluate the long-term stability and anti-fouling properties of these coatings under continuous flow conditions and investigate the impact of varying concentrations of dissolved organic matter (DOM) and inorganic ions on the catalyst's active sites over extended operational cycles.
5. Broadening the Pollutant Scope: Expanding the application of these electrodeposited copper oxide films to other emerging contaminants, such as sulfamethoxazole and carbamazepine, would help determine the versatility of the CuO/Cu_2O heterojunction for broad-spectrum wastewater remediation.

4. Conclusions

This study successfully demonstrates a low-temperature, energy-efficient strategy for fabricating mixed-phase copper oxide (CuO/Cu_2O) photocatalysts tailored for the degradation of recalcitrant antibiotics. The research highlights that the precursor aging time is a critical synthesis parameter; a 25 min aging period (T25) preserves a metastable multi-phase composition with high structural disorder and nanocrystalline domains, whereas 35 min (T35) promotes phase consolidation toward bulk crystalline CuO, reducing the density of active catalytic sites. Granulometric analysis of the T25 precursor displayed a mean diameter of 1.25 μm and a high specific surface area of 23,955.20 cm^2/g, which provided a robust colloidal foundation for immobilization via electrophoretic deposition (EPD).

The optimization of EPD parameters revealed that the applied voltage serves as an influencer of the phase composition and deposition and also a crystallization driver. While the 0.9 V condition achieved the highest fidelity (42%) to the original T25 mixed-phase structure, the 1.0 V condition was identified as the optimal balance, promoting selective Cu_2O enrichment—transferring 2.6 times more efficiently than CuO—and in situ crystal growth, resulting in significantly larger crystallites (up to 99.0 nm) that enhance mechanical

and photo-corrosion stability. In contrast, the 1.2 V condition, though producing the smallest nanocrystals (19.4 nm), was limited by a lack of phase diversity, being dominated almost entirely by Cu_2O.

The photocatalytic performance assessments underscore a clear distinction between initial transformation speed and deep mineralization. In a complex, biologically treated wastewater matrix spiked with ciprofloxacin, the 1.2 V catalyst displayed rapid 5 min transformation, reducing the parent compound signal to its lowest level (~50.6 mAU). However, the 0.9 V catalyst achieved the highest degree of mineralization (18% TOC removal), whereas higher voltages were hampered by parasitic oxygen evolution reactions. Adsorption experiments further indicated that surface chemistry and mixed-phase heterojunctions dominate over simple surface area effects, as the 0.9 V and 1.0 V films outperformed the 1.2 V film in antibiotic uptake despite having larger crystallite sizes.

HPLC-MS analysis suggested a comprehensive degradation pathway proceeding through piperazine ring cleavage, defluorination, and quinolone core destruction, evidenced by the formation of intermediates such as m/z 305, 288, 185, and 143. While complete mineralization was not achieved within the tested timeframes, the structural fragmentation of ciprofloxacin into stable, low-molecular-weight intermediates suggests the efficacy of these CuO/Cu_2O coatings. Ultimately, this integrated approach—combining controlled low-temperature synthesis with tuned EPD—offers a sustainable and scalable pathway for developing high-performance photocatalytic surfaces capable of remediating emerging contaminants in real-world aquatic environments. These findings establish applied voltage as a critical design parameter for tuning phase composition, degradation pathways, and mineralization efficiency in CuO/Cu_2O photocatalytic systems.

Supplementary Materials: The following supporting information can be downloaded at https://www.mdpi.com/article/10.3390/coatings16080982/s1. Figure S1: Ambient temperature air dried powder; Figure S2: Low-temperature dried powder without aging; Figure S3: Aged precursor powders: T25, T35 and T60; Figure S4: Schematic illustration of the experimentally observed copper phase evolution during precursor aging, low-temperature drying, and electrophoretic deposition; Table S1: Estimated Phase Composition as a Function of Aging Condition; Table S2: Literature comparison of Cu_2O/Cu formation without conventional reducing agents.

Author Contributions: Conceptualization, M.-A.O.O.-A. and A.Š.; Methodology, M.-A.O.O.-A.; Software, B.A. and A.Š.; Validation, A.G. and A.Š.; Formal analysis, A.G.; Investigation, M.-A.O.O.-A., A.G. and B.A.; Resources, B.A. and A.Š.; Writing—original draft, M.-A.O.O.-A. and A.G.; Writing—review & editing, M.-A.O.O.-A., B.A. and A.Š.; Visualization, B.A. and A.Š.; Supervision, A.Š.; Project administration, A.Š. All authors have read and agreed to the published version of the manuscript.

Funding: This research received no external funding.

Institutional Review Board Statement: Not applicable.

Informed Consent Statement: Not applicable.

Data Availability Statement: The data presented in this study are available from the corresponding author upon reasonable request.

Acknowledgments: The authors would like to thank the Department of Physical and Inorganic Chemistry at the Kaunas University of Technology for providing the research facilities and technical support necessary for this work. We extend our sincere gratitude to Brigita Abakevičienė for providing the materials science data and technical information essential to this study. Special thanks are also given to Agnė Šulčiūtė for her supervision and guidance throughout the research process.

Conflicts of Interest: The authors declare no conflict of interest.

References

1. Mashentseva, A.A.; Nurpeisova, D.T.; Barsbay, M. Effect of copper doping on the photocatalytic performance of Ni2O3 @PC membrane composites in norfloxacin degradation. *RSC Adv.* **2024**, *14*, 4424–4435. [CrossRef] [PubMed]
2. Jiang, W.; Sukhotu, R.; Huang, Y.; Chen, J.; Li, F.; Yang, J. Solvothermal preparation of CuO/g-C3N4 and photocatalytic degradation of ciprofloxacin. *J. Dispers. Sci. Technol.* **2024**, *46*, 1–12. [CrossRef]
3. Jia, X.; Zhang, J.; Huang, Q.; Xiong, C.; Ji, H.; Ren, Q.; Jin, Z.; Chen, S.; Guo, W.; Chen, J.; et al. Efficient degradation of ciprofloxacin in wastewater by $CuFe_2O_4$/CuS photocatalyst activated peroxynomosulfate. *Environ. Res.* **2024**, *241*, 117639. [CrossRef] [PubMed]
4. Onoriode-Afunezie, M.-A.O.; Urbanskis, P.; Urniežaitė, I.; Šulčiūtė, A. Optimized TiO2 Coatings on AISI 316 Steel for Advanced Photocatalytic Wastewater Treatment: Mechanism and Performance. *ACS Omega* **2025**, *10*, 34666–34682. [CrossRef] [PubMed]
5. Długosz, O.; Lis, K.; Matyjasik, W.; Radomski, P.; Pulit-Prociak, J.; Banach, M. Cu_2O Nanoparticles Deposited on Y2O3 and CuO: Synthesis and Antimicrobial Properties. *J. Clust. Sci.* **2023**, *34*, 2153–2165. [CrossRef]
6. Tabassum, S.; Hossain, M.S.; Abu Saeed, M.; Uddin, M.N.; Ahmed, S. Exploration of the antibacterial and photocatalytic properties of copper oxide (CuO) nanoparticles synthesized from *Azadirachta indica* leaf extract and electronic waste cable. *Mater. Adv.* **2025**, *6*, 2338–2355. [CrossRef]
7. Yu, X.; Zhao, C.; Liu, Z.; Wei, Y.; Yang, M.; Guo, B.; Niu, J. Preparation of ZnO/Cu_2O Composite Particles and Its Degradation of Ciprofloxacin: Analysis of Degradation Performance and Active Species. *Integr. Ferroelectr.* **2023**, *236*, 96–108. [CrossRef]
8. Khiavi, N.D.; Katal, R.; Eshkalak, S.K.; Masudy-Panah, S.; Ramakrishna, S.; Jiangyong, H. Visible Light Driven Heterojunction Photocatalyst of CuO–Cu_2O Thin Films for Photocatalytic Degradation of Organic Pollutants. *Nanomaterials* **2019**, *9*, 1011. [CrossRef] [PubMed]
9. Motshekga, S.C. Structural and antibacterial properties of copper oxide nanoparticles: A study on the effect of calcination temperature. *Nano Express* **2024**, *5*, 015011. [CrossRef]
10. Akhtar, M.A.; Ilyas, K.; Dlouhý, I.; Siska, F.; Boccaccini, A.R. Electrophoretic Deposition of Copper(II)–Chitosan Complexes for Antibacterial Coatings. *Int. J. Mol. Sci.* **2020**, *21*, 2637. [CrossRef] [PubMed]
11. Besra, L.; Liu, M. A review on fundamentals and applications of electrophoretic deposition (EPD). *Prog. Mater. Sci.* **2007**, *52*, 1–61. [CrossRef]
12. Boccaccini, A.R.; Keim, S.; Ma, R.; Li, Y.; Zhitomirsky, I. Electrophoretic deposition of biomaterials. *J. R. Soc. Interface* **2010**, *7*, S581–S613. [CrossRef] [PubMed]
13. Shehayeb, S.; Deschanels, X.; Karamé, I.; Ghannam, L.; Toquer, G. Spectrally selective coatings obtained from electrophoretic deposition of CuO nanoparticles. *Surf. Coat. Technol.* **2017**, *322*, 38–45. [CrossRef]
14. Van der Biest, O.O.; Vandeperre, L.J. Electrophoretic deposition of materials. *Annu. Rev. Mater. Sci.* **1999**, *29*, 327–352. [CrossRef]
15. Zhitomirsky, I. Cathodic electrodeposition of ceramic and organoceramic materials. Fundamental aspects. *Adv. Colloid Interface Sci.* **2002**, *97*, 279–317. [CrossRef] [PubMed]
16. Killian, M.S.; Wagener, V.; Schmuki, P.; Virtanen, S. Functionalization of Metallic Magnesium with Protein Layers via Linker Molecules. *Langmuir* **2010**, *26*, 12044–12048. [CrossRef] [PubMed]
17. Bin Chan, Y.; Selvanathan, V.; Tey, L.-H.; Akhtaruzzaman; Anur, F.H.; Djearamane, S.; Watanabe, A.; Aminuzzaman, M. Effect of Calcination Temperature on Structural, Morphological and Optical Properties of Copper Oxide Nanostructures Derived from *Garcinia mangostana* L. Leaf Extract. *Nanomaterials* **2022**, *12*, 3589. [CrossRef] [PubMed]
18. Saberian, M.; Nezamzadeh-Ejhieh, A. Synergistic photocatalytic degraded tetracycline upon supported CuO clinoptilolite nanoparticles. *Solid State Sci.* **2024**, *147*, 107381. [CrossRef]
19. Agalya, P.; Suresh, S.; Prabu, K.; Thambidurai, S.; Kandasamy, M.; Kumar, S.K.; Pugazhenthiran, N. Facile and low-cost synthesis of diverse copper oxide nanostructures for solar to thermal energy conversion. *Optik* **2021**, *244*, 167499. [CrossRef]
20. Sorkhi, L.; Farrokhi-Rad, M.; Shahrabi, T. Electrophoretic Deposition of Hydroxyapatite–Chitosan–Titania on Stainless Steel 316 L. *Surfaces* **2019**, *2*, 458–467. [CrossRef]
21. Wongchaiya, P.; Nguyen, T.K.N.; Sujaridworakun, P.; Larpkiattaworn, S.; Suzuki, T.S.; Uchikoshi, T. Fabrication of g-C3N4 films with enhanced mechanical and charge transfer properties by electrophoretic deposition and subsequent citric acid modification. *Adv. Powder Technol.* **2024**, *35*, 104460. [CrossRef]
22. Yang, J.H.C.; Wu, S.-L.; Tsai, C. Green and rapid fabrication of copper oxide in enhanced electrode liquid phase plasma system. *Plasma Process. Polym.* **2022**, *19*, 2200078. [CrossRef]
23. Díaz-Reyes, J.; Castillo-Ojeda, R.S.; Galván-Arellano, M.; Flores-Mena, J.E. Growth and Characterization of (CuXO (X=1,2) Nanocrystalline Layers Grown on Silicon Deposited by Thermal Copper Oxidation. *Mex. J. Mat. Sci. Eng.* **2014**, *1*, 46–51.
24. Shahsavani, E.; Feizi, N.; Khalaji, A.D. Copper Oxide Nanoparticles Prepared by Solid State Thermal Decomposition: Synthesis and Characterization. *Front. Manuf. Eng.* **2016**, *4*, 48. [CrossRef]
25. Al-Saeedi, S.I.; Al-Senani, G.M.; Abd-Elkader, O.H.; Deraz, N.M. One Pot Synthesis, Surface and Magnetic Properties of Cu_2O/Cu and Cu_2O/CuO Nanocomposites. *Crystals* **2021**, *11*, 751. [CrossRef]

26. Ivanauskas, R.; Ancutienė, I.; Milašienė, D.; Ivanauskas, A.; Bronušienė, A. Effect of Reducing Agent on Characteristics and Antibacterial Activity of Copper-Containing Particles in Textile Materials. *Materials* **2022**, *15*, 7623. [CrossRef] [PubMed]
27. Sahu, K.; Choudhary, S.; Khan, S.A.; Pandey, A.; Mohapatra, S. Thermal evolution of morphological, structural, optical and photocatalytic properties of CuO thin films. *Nano-Struct. Nano-Objects* **2019**, *17*, 92–102. [CrossRef]
28. Rehman, S.; Akhtar, S.N.; Munir, S.M.; Ali, K.; Javed, Y.; Jamil, Y.; Sajjad, M.; Nawaz, A.; Kumar, S.S. Tuning Structural and Optical Properties of Copper Oxide Nanomaterials by Thermal Heating and Its Effect on Photocatalytic Degradation of Congo Red Dye. *Iran. J. Chem. Chem. Eng.* **2022**, *41*, 1549–1560.
29. Li, Y.; Chen, X.; Li, L. Facile thermal exfoliation of Cu sheets towards the CuO/Cu_2O heterojunction: A cost-effective photocatalyst with visible-light response for promising sustainable applications. *RSC Adv.* **2019**, *9*, 33395–33402. [CrossRef] [PubMed]
30. Li, X.; Zhang, C.; Yang, Q.; Zhao, R.; Li, H. Facile regulation of cuprous oxide microcrystal morphology and planes for visible light photocatalytic degradation. *Micro Nano Lett.* **2022**, *17*, 327–335. [CrossRef]
31. Budi, S.; Takahashi, M.; Sutrisno, M.G.; Adi, W.A.; Fairuza, Z.; Kurniawan, B.; Maenosono, S.; Umar, A.A. Phases evolution and photocatalytic activity of Cu_2O films electrodeposited from a non-pH-adjusted solution. *R. Soc. Open Sci.* **2023**, *10*, 230247. [CrossRef] [PubMed]
32. Mateo, D.; Esteve-Adell, I.; Albero, J.; Primo, A.; García, H. Oriented 2.0.0 Cu_2O nanoplatelets supported on few-layers graphene as efficient visible light photocatalyst for overall water splitting. *Appl. Catal. B Environ.* **2017**, *201*, 582–590. [CrossRef]
33. Khasanah, R.A.N.; Lin, H.-C.; Ho, H.-Y.; Peng, Y.-P.; Lim, T.-S.; Hsiao, H.-L.; Wang, C.-R.; Chuang, M.-C.; Chien, F.S.-S. Studies on the substrate-dependent photocatalytic properties of Cu_2O heterojunctions. *RSC Adv.* **2021**, *11*, 4935–4941. [CrossRef] [PubMed]
34. Bayat, F.; Sheibani, S. Enhancement of photocatalytic activity of CuO-Cu_2O heterostructures through the controlled content of Cu_2O. *Mater. Res. Bull.* **2022**, *145*, 111561. [CrossRef]
35. Tang, Q.; Wu, W.; Zhang, B.; Luo, J.; Zhang, H.; Guo, X.; Jia, J.; Cao, J. A Novel In Situ Synthesis of Cu/Cu_2O/CuO/Sulfonated Polystyrene Heterojunction Photocatalyst with Enhanced Photodegradation Activity. *J. Inorg. Organomet. Polym. Mater.* **2019**, *29*, 340–345. [CrossRef]
36. Han, L.; Zhan, W.; Liang, X.; Zhang, W.; Huang, R.; Chen, R.; Ni, H. In-situ generation Cu_2O/CuO core-shell heterostructure based on copper oxide nanowires with enhanced visible-light photocatalytic antibacterial activity. *Ceram. Int.* **2022**, *48*, 22018–22030. [CrossRef]
37. Uschakov, A.; Karpov, I.; Lepeshev, A.; Zharkov, S. The Influence of Oxygen Concentration on the Formation of CuO and Cu_2O Crystalline Phases during the Synthesis in the Plasma of Low Pressure Arc Discharge. *Vacuum* **2016**, *128*, 123–127. [CrossRef]
38. Karpov, I.V.; Ushakov, A.V. Synthesis of Metal-Organic Framework Structures Based on Copper in a Low-Pressure Arc Discharge Plasma. *Int. J. Nanosci.* **2020**, *19*, 2050003. [CrossRef]
39. Sterzinger, J.; Gulie, B.; Maier, V.; Steeger, T.; Peters, C.; Patelis, N.; Gubanova, E.; Willinger, M.; Bandarenka, A.S. Size-Dependent Oxidation of Copper Nanostructured Electrocatalysts Produced by Spark Ablation. *ACS Electrochem* **2026**, *2*, 1397–1405. [CrossRef] [PubMed]
40. Luciano, V.A.; Perígolo, D.M.; Rosmaninho, M.G.; Teixeira, A.P.C. Production of Fuels via Thermal Decomposition of Copper Oleates from CuO. *Fuel* **2020**, *261*, 116456. [CrossRef]
41. Sun, K.; Hu, H.; He, Z.; Xiao, Z.; Jin, X.; Zheng, C.; Liu, Y. 'One-pot green solid-state synthesis of Cu_2O/microcrystalline cellulose composite with high an-ti-pathogenic activity'. *Carbohydr. Polym.* **2024**, *332*, 121851. [CrossRef] [PubMed]
42. D, M.; Peddi, K.M.; R, R. CuO Nanoparticles: Synthesis, Characterization and Their Bactericidal Efficacy. *Int. J. Appl. Pharm.* **2017**, *9*, 71–74. [CrossRef]
43. Kayani, Z.N.; Umer, M.; Riaz, S.; Naseem, S. Characterization of Copper Oxide Nanoparticles Fabricated by the Sol–Gel Method. *J. Electron. Mater.* **2015**, *44*, 3704–3709. [CrossRef]
44. Rahnama, A.; Gharagozlou, M. Preparation and properties of semiconductor CuO nanoparticles via a simple precipitation method at different reaction temperatures. *Opt. Quantum Electron.* **2012**, *44*, 313–322. [CrossRef]
45. Kartal, C.; Hanedar, Y.; Öznülüer, T.; Demir, Ü. Stoichiometry, Morphology, and Size-Controlled Electrochemical Fabrication of CuxO (x = 1, 2) at Underpotential. *Langmuir* **2017**, *33*, 3960–3967. [CrossRef] [PubMed]
46. Ganesan, K.P.; Anandhan, N.; Marimuthu, T.; Panneerselvam, R.; Roselin, A.A. Effect of Deposition Potential on Synthesis, Structural, Morphological and Photoconductivity Response of Cu_2O Thin Films by Electrodeposition Technique. *Acta Met. Sin. (Engl. Lett.)* **2019**, *32*, 1065–1074. [CrossRef]
47. Farhad, S.F.U.; Hossain, M.; Bashar, M.S.; Tanvir, N.I.; Islam, S. Communication—Texture and Bandgap Tuning of Phase Pure Cu_2O Thin Films Grown by a Simple Potentiostatic Electrodeposition Technique. *ECS Adv.* **2024**, *3*, 013001. [CrossRef]
48. Izaki, M.; Abe, S.; Nakakita, K.; Khoo, P.L. Photoelctrochemically Fabricated and Heated Cu_2O/CuO Bilayers with Enhanced Photovoltaic Characteristics. *ACS Omega* **2021**, *6*, 27587–27597. [CrossRef] [PubMed]
49. Zahra, S.N.; Wulandari, F.; Rauf, M.R.; Arum, A. Decorating Cu_2O with Copper Metal (Cu) through Facile Electrochemical Deposition for Methylene Blue Degradation. *Chem. Mater.* **2024**, *3*, 71–80. [CrossRef]

50. Riveros, G.; León, M.; Ramírez, D. Effect of Chloride Ions on the Structural, Optical, Morphological, and Electrochemical Properties of Cu_2O Films Electrodeposited on Fluorine-Doped Tin Oxide Substrate from a DMSO Solution. *J. Chil. Chem. Soc.* **2016**, *61*, 3219–3223. [CrossRef]
51. Reppin, D.; Polity, A.; Meyer, B.K.; Shokhovets, S. Optical and electrical properties of Cu_2O, Cu_4O_3 and CuO. *MRS Proc.* **2012**, *1494*, 165–169. [CrossRef]
52. Derbal, S.; Benaicha, M. Insights on the Effect of Applied Potential on the Properties of Electrodeposited p-Type Cuprous Oxide (Cu_2O) Thin Films. *J. Electron. Mater.* **2021**, *50*, 5134–5140. [CrossRef]
53. Tomar, L.J.; Desai, R.K.; Chakrabarty, B.S. Study of optical properties of hydrothermally synthesized $Cu/Cu_2O/CuO$ nanocrystals. *AIP Conf. Proc.* **2013**, *1536*, 245–246. [CrossRef]
54. Yan, B.; Wang, Y.; Jiang, T.; Wu, X. Fabrication of snowflake-like CuO nanostructure via electrodeposition method and its properties. *J. Mater. Sci. Mater. Electron.* **2016**, *27*, 4035–4042. [CrossRef]
55. Bouzekri, O.; El Gamouz, S.; Ed-Dra, A.; Moussout, H.; Dehmani, Y.; Ziyat, H.; El Idrissi, M.; Choukrad, M.; Abouarnadasse, S. Green Synthesis of Nickel and Copper Nanoparticles Doped with Silver from *Hammada scoparia* Leaf Extract and Evaluation of Their Potential to Inhibit Microorganisms and to Remove Dyes from Aqueous Solutions. *Sustainability* **2023**, *15*, 1541. [CrossRef]
56. Khan, A.; Rashid, A.; Younas, R.; Chong, R. A chemical reduction approach to the synthesis of copper nanoparticles. *Int. Nano Lett.* **2016**, *6*, 21–26. [CrossRef]
57. Wang, G.; van den Berg, C.; de Mello Donega, C.; de Jong, K.P.; de Jongh, P.E. Silica-supported Cu_2O nanoparticles with tunable size for sustainable hydrogen generation. *Appl. Catal. B Environ.* **2016**, *192*, 199–207. [CrossRef]
58. Yang, X.; Zhang, S.; Zhang, L.; Zhang, B.; Ren, T. Dynamic growth of rhombic dodecahedral Cu_2O crystals controlled by reaction temperature and their size-dependent photocatalytic performance. *RSC Adv.* **2019**, *9*, 36831–36837. [CrossRef] [PubMed]
59. Van Tran, T.; Nguyen, D.T.C.; Nguyen, T.T.; Le, H.T.; Van Nguyen, C.; Nguyen, T.D. Metal-organic framework HKUST-1-based $Cu/Cu_2O/CuO$@C porous composite: Rapid synthesis and uptake application in antibiotics remediation. *J. Water Process. Eng.* **2020**, *36*, 101319. [CrossRef]
60. Liu, G.; Liu, Z.; Li, S.; Shi, C.; Xu, T.; Huo, M.; Lin, Y. Aluminum copper bimetallic metal organic gels/sodium alginate beads for efficient adsorption of ciprofloxacin and methylene blue: Adsorption isotherm, kinetic and mechanism studies. *Process. Saf. Environ. Prot.* **2023**, *176*, 763–775. [CrossRef]
61. Bhattacharya, P.; Mukherjee, D.; Dey, S.; Ghosh, S.; Banerjee, S. Development and performance evaluation of a novel CuO/TiO_2 ceramic ultrafiltration membrane for ciprofloxacin removal. *Mater. Chem. Phys.* **2019**, *229*, 106–116. [CrossRef]
62. Umeh, C.T.; Nduka, J.K.; Akpomie, K.G.; Ighalo, J.O.; Mogale, R. Adsorptive Effect of Corn Silk-Loaded Nickel Oxide and Copper Oxide Nanoparticles for Elimination of Ciprofloxacin from Wastewater. *ACS Omega* **2025**, *10*, 3784–3800. [CrossRef] [PubMed]
63. Zheng, K.; Zheng, X.; Yu, F.; Ma, J. Removal of ciprofloxacin from aqueous solution using long TiO_2 nanotubes with a high specific surface area. *RSC Adv.* **2016**, *6*, 3625–3631. [CrossRef]
64. Ahmadi, S.; Banach, A.; Mostafapour, F.K.; Balarak, D. Study survey of cupric oxide nanoparticles in removal efficiency of ciprofloxacin antibiotic from aqueous solution: Adsorption isotherm study. *Desalin. Water Treat.* **2017**, *89*, 297–303. [CrossRef]
65. Mohammed, A.A.; Kareem, S.L. Enhancement of ciprofloxacin antibiotic removal from aqueous solution using ZnO nanoparticles coated on pistachio shell. *Desalin. Water Treat.* **2021**, *213*, 229–239. [CrossRef]
66. Villegas-Guzman, P.; Oppenheimer-Barrot, S.; Silva-Agredo, J.; Torres-Palma, R.A. Comparative Evaluation of Photo-Chemical AOPs for Ciprofoxacin Degradation: Elimination in Natural Waters and Analysis of pH Effect, Primary Degradation By-Products, and the Relationship with the Antibiotic Activity. *Water Air Soil Pollut.* **2017**, *228*, 209. [CrossRef]
67. Lu, C.; Gu, J.; Wei, G.; Ba, J.; Zhang, L.; Li, Z.; Pei, R.; Li, J.; Wei, J. Three-Dimensional Electro-Fenton Degradation of Ciprofloxacin Catalyzed by Cuo Doped Red Mud Particle Electrodes: Influencing Factors, Possible Degradation Pathways and Energy Consumption. *J. Environ. Chem. Eng.* **2022**, *10*, 107737. [CrossRef]
68. Zhang, T.; Zhang, J.; Yu, Y.; Li, J.; Zhou, Z.; Li, C. Synthesis of CuO/GO-DE Catalyst and Its Catalytic Properties and Mechanism on Ciprofloxacin Degradation. *Nanomaterials* **2022**, *12*, 4305. [CrossRef] [PubMed]
69. Shen, J.-H.; Chiang, T.-H.; Tsai, C.-K.; Jiang, Z.-W.; Horng, J.-J. Mechanistic insights into hydroxyl radical formation of Cu-doped ZnO/g-C3N4 composite photocatalysis for enhanced degradation of ciprofloxacin under visible light: Efficiency, kinetics, products identification and toxicity evaluation. *J. Environ. Chem. Eng.* **2022**, *10*, 107352. [CrossRef]
70. Zeng, Y.; Zhou, G.; He, D.; Peng, G. Catalytic Degradation of Ciprofloxacin in Aqueous Solution by Peroxymonosulfate Activated with a Magnetic $CuFe_2O_4$@Biochar Composite. *Int. J. Mol. Sci.* **2023**, *24*, 5702. [CrossRef] [PubMed]
71. Tsai, C.-K.; Huang, C.-H.; Horng, J.-J.; Ong, H.L.; Doong, R.-A. Enhanced Visible-Light-Responsive Photocatalytic Degradation of Ciprofloxacin by the CuxO/Metal-Organic Framework Hybrid Nanocomposite. *Nanomaterials* **2023**, *13*, 282. [CrossRef] [PubMed]
72. Zhu, W.; Du, J.; Yang, Q. Construction of a Double Z-Scheme $CuO/Cu_2O/CuS/ZnO$ Quaternary Heterojunction Photocatalyst with Enhanced Solar-Driven Photocatalytic Performance for Sulfamethoxazole Degradation. *ChemistrySelect* **2024**, *9*, e202400261. [CrossRef]

73. Kumar, S.; Bhawna; Gupta, A.; Kumar, R.; Bharti, A.; Kumar, A.; Kumar, V. New Insights into Cu/Cu_2O/CuO Nanocomposite Heterojunction Facilitating Photocatalytic Generation of Green Fuel and Detoxification of Organic Pollutants. *J. Phys. Chem. C* **2023**, *127*, 7095–7106. [CrossRef]
74. Abromaitis, V.; Svaikauskaite, J.; Sulciute, A.; Sinkeviciute, D.; Zmuidzinaviciene, N.; Misevicius, S.; Tichonovas, M.; Urniezaite, I.; Jankunaite, D.; Urbonavicius, M.; et al. Ozone-enhanced TiO_2 nanotube arrays for the removal of COVID-19 aided antibiotic ciprofloxacin from water: Process implications and toxicological evaluation. *J. Environ. Manag.* **2022**, *318*, 115515. [CrossRef] [PubMed]
75. Nair, N.; Gandhi, V.; Shukla, A.; Ghotekar, S.; Nguyen, V.-H.; Varma, K. Mechanisms in the photocatalytic breakdown of persistent pharmaceutical and pesticide molecules over TiO_2-based photocatalysts: A review. *J. Phys. Condens. Matter* **2024**, *36*, 413003. [CrossRef] [PubMed]
76. Usman, M.R.; Prasasti, A.; Islamiah, S.; Firdaus, A.N.; Marita, A.W.; Fajriyah, S.; Noviyanti, A.R.; Eddy, D.R. Degradation of Ciprofloxacin by Titanium Dioxide (TiO_2) Nanoparticles: Optimization of Conditions, Toxicity, and Degradation Pathway. *Bull. Chem. React. Eng. Catal.* **2021**, *16*, 752–762. [CrossRef]
77. Zhou, Z.; Jiang, J.-Q. Reaction kinetics and oxidation products formation in the degradation of ciprofloxacin and ibuprofen by ferrate(VI). *Chemosphere* **2015**, *119*, S95–S100. [CrossRef] [PubMed]
78. Wachter, N.; Aquino, J.M.; Denadai, M.; Barreiro, J.C.; Silva, A.J.; Cass, Q.B.; Rocha-Filho, R.C.; Bocchi, N. Optimization of the electrochemical degradation process of the antibiotic ciprofloxacin using a double-sided β-PbO_2 anode in a flow reactor: Kinetics, identification of oxidation intermediates and toxicity evaluation. *Environ. Sci. Pollut. Res.* **2019**, *26*, 4438–4449. [CrossRef] [PubMed]
79. Liu, Y.; Kamali, M.; Chen, X.; Rossi, B.; Appels, L.; Dewil, R. Photocatalytic defluorination of ciprofloxacin by nitrogen-defected g-C3N4 under simulated sunlight: Mechanistic insight and pathway analysis. *Chem. Eng. J.* **2024**, *493*, 151950. [CrossRef]